Lag structure in resting-state fMRI

A. Mitra,[✉][1] A. Z. Snyder,[1,3] C. D. Hacker,[2] and M. E. Raichle[1,3]

[1]Department of Radiology, Washington University, St. Louis, Missouri;

[2]Department of Biomedical Engineering, Washington University, St. Louis, Missouri; and

[3]Department of Neurology, Washington University, St. Louis, Missouri

[✉]Corresponding author.

Address for reprint requests and other correspondence: A. Mitra, Dept. of Radiology, Washington Univ., 4525 Scott Ave., St. Louis, MO 63110 (e-mail: anishmitra@wustl.edu).

Abstract

The discovery that spontaneous fluctuations in blood oxygen level-dependent (BOLD) signals contain information about the functional organization of the brain has caused a paradigm shift in neuroimaging. It is now well established that intrinsic brain activity is organized into spatially segregated resting-state networks (RSNs). Less is known regarding how spatially segregated networks are integrated by the propagation of intrinsic activity over time. To explore this question, we examined the latency structure of spontaneous fluctuations in the fMRI BOLD signal. Our data reveal that intrinsic activity propagates through and across networks on a timescale of ~1 s. Variations in the latency structure of this activity resulting from sensory state manipulation (eyes open vs. closed), antecedent motor task (button press) performance, and time of day (morning vs. evening) suggest that BOLD signal lags reflect neuronal processes rather than hemodynamic delay. Our results emphasize the importance of the temporal structure of the brain's spontaneous activity.

IT HAS BEEN RECOGNIZED since the inception of fMRI that the blood oxygen level-dependent (BOLD) signal exhibits spontaneous fluctuations (Purdon and Weisskoff 1998). Although this phenomenon was initially regarded as noise, Biswal and colleagues showed that spontaneous fluctuations of the BOLD signal are temporally synchronous within the somatomotor system (Biswal et al. 1995). This basic result has since been extended to multiple functional systems spanning the entire brain (Buckner et al. 2011; Choi et al. 2012; Power et al. 2011; Yeo et al. 2011). Synchronicity

of intrinsic activity is widely referred to as functional connectivity; the associated topographies are known as resting-state networks [RSNs; equivalently, intrinsic connectivity networks (Fox and Raichle 2007)]. The importance of understanding intrinsic activity is underscored by the fact that RSNs recapitulate the topographies of fMRI responses to a wide variety of sensory, motor, and cognitive task paradigms (Cordes et al. 2000; Smith et al. 2009), providing a powerful means of delineating brain functional organization without the need for subjects to perform tasks. RSNs also provide an important window on the pathophysiology of various diseases (Fox and Greicius 2010; Zhang and Raichle 2010). These results establish that intrinsic brain activity is spatially structured, linked to the representation of function, and clinically relevant.

Almost all prior fMRI studies of intrinsic brain activity have used either seed-based correlation mapping (Biswal et al. 2010) or spatial independent components analysis (sICA) (Beckmann et al. 2005). Critically, both of these computational strategies incorporate the assumption that activity within RSNs is exactly synchronous. However, resting-state fMRI studies in rat and human suggest that intrinsic activity is spatiotemporally structured (Majeed et al. 2009, 2011). Ample evidence of temporally structured intrinsic activity has been observed in the mouse with voltage-sensitive dye (VSD) imaging (Ferezou et al. 2007; Han et al. 2008; Huang et al. 2010; Mohajerani et al. 2010, 2013; Sato et al. 2012). In humans, Garg and colleagues (Garg et al. 2011) performed vector auto-regressive (VAR) modeling of intrinsic activity followed by dimensionality reduction and identified two main spatiotemporal streams propagating through the brain. More recently, Smith and colleagues (Smith et al. 2012) used temporal independent component analysis (tICA) to isolate multiple "temporal functional modes" in human resting-state fMRI data. Implicit in this analysis is the notion that intrinsic brain activity can be decomposed into spatiotemporal components. However, the temporal features of these components were not explicitly explored.

Here we specifically focus on the temporal features of intrinsic brain activity as expressed in its latency structure. We demonstrate that lags in intrinsic activity, as reflected in the BOLD signal, are highly reproducible across several large cohorts of young healthy adults. Moreover, this structure is modified, with appropriate focality, by the state of the eyes (open or closed), recent motor task performance, and time of day (i.e., morning vs. evening). When represented in three-dimensional (3D) image format, iso-lag contours superficially resemble RSNs. However, closer analysis shows that lag topography actually is orthogonal to RSNs. Thus each RSN encompasses a range of early and late regions, and no RSN leads or follows any other. Rather, a temporal structure emerges that provides a framework for the functional integration of more conventionally defined RSNs.

THEORY

Conventional seed-based correlation analysis involves computation of the Pearson correlation, r, between the time series extracted from a seed region, e.g., $x_1(t)$, and a second time series, $x_2(t)$, extracted from other loci [either single voxels or another region of interest (ROI)]. Thus

$$r_{x_1 x_2} = \frac{1}{\sigma_{x_1} \sigma_{x_2}} \frac{1}{T} \int x_1(t) \cdot x_2(t) dt \tag{1}$$

where σ_{x_1} and σ_{x_2} are the temporal standard deviations of signals x_1 and x_2 and T is the interval of integration. Here we generalize the assumption of exact temporal synchrony and compute lagged cross-covariance functions. Thus

$$C_{x_1 x_2}(\tau) = \frac{1}{T} \int x_1(t+\tau) \cdot x_2(t) \, dt \tag{2}$$

where τ is the lag (in units of time). The value of τ at which $C_{x_1 x_2}(\tau)$ exhibits an extremum defines the temporal lag (equivalently, delay) between signals x_1 and x_2 ([Konig 1994](#)). (Alternative strategies for latency analysis are discussed in APPENDIX.) Clearly, *Eqs. 1* and *2* are related. Thus $C_{x_1 x_2}(0)$ = $\sigma_{x_1} \sigma_{x_2} r_{x_1 x_2}$. In other words, the Pearson correlation is equal to the cross-covariance at zero lag, normalized by the signal standard deviations. Because cross-covariance functions are not normalized, they retain sensitivity to signal magnitudes, which is critical in the present analyses. Although cross-covariance functions can exhibit multiple extrema in the analysis of periodic signals, BOLD time series are aperiodic ([He et al. 2010](#); [Maxim et al. 2005](#)) and almost always give rise to lagged cross-covariance functions with a single, well-defined extremum, typically in the range ±0.5 s. We determined the x- and y-coordinates of the extremum using parabolic interpolation ([Fig. 1](#)).

Given a set of n time series, $\{x_1(t), x_2(t), \ldots, x_n(t)\}$, extracted from n ROIs, a lagged cross-covariance function can be computed between every pair of time series. Thus

$$C_{x_i x_j}(\tau) = \frac{1}{T} \int x_i(t+\tau) \cdot x_j(t) \, dt \quad i,j \in 1,2,\ldots,n \tag{3}$$

$C_{xx}(\tau)$ is an $n \times n$ matrix that describes the covariance structure of the signal system parametric in lag. Finding all τ_{ij} corresponding to the extrema, a_{ij}, of $C_{x_i x_j}(\tau)$ yields the anti-symmetric matrix, T:

$$T = \begin{bmatrix} \tau_{1,1} & \cdots & \tau_{1,n} \\ \vdots & \ddots & \vdots \\ -\tau_{1,n} & \cdots & \tau_{n,n} \end{bmatrix} \tag{4}$$

The diagonal entries of T are necessarily zero, as any time series has zero lag with itself. Moreover, $\tau_{ij} = -\tau_{j,i}$, since time series $x_i(t)$ preceding $x_j(t)$ implies that $x_j(t)$ follows $x_i(t)$ by the same interval. T is widely known as a time-delay (TD) matrix and represents all lag information contained in $\{x_1(t), x_2(t), \ldots, x_n(t)\}$.

The TD matrix does not contain any information regarding signal magnitudes. Therefore, the relative contribution of each signal pair to the entire spatiotemporal process is lost. To recover signal magnitude information, we define a second anti-symmetric matrix, A:

$$A = \begin{bmatrix} \tau_{1,1} \cdot a_{1,1} & \cdots & \tau_{1,n} \cdot a_{1,n} \\ \vdots & \ddots & \vdots \\ -\tau_{1,n} \cdot a_{1,n} & \cdots & \tau_{n,n} \cdot a_{n,n} \end{bmatrix} \tag{5}$$

A is anti-symmetric for the same reasons as T is. In A, the time delays, τ_{ij}, are weighted by the magnitude of the signals at the extremum of $C_{x_i x_j}(\tau)$. We refer to A as an amplitude-weighted time-delay (AWTD) matrix.

We projected the multivariate data represented in the TD and AWTD matrices onto one-dimensional (1D) maps, using the technique described by Nikolic and colleagues ([Nikolic 2007](); [Schneider et al. 2006]()). We refer to these 1D maps as latency projections. Operationally, the projection is done by taking the mean across the columns of T ([Eq. 4]()) and A ([Eq. 5]()), that is,

$$T_p = (1/n) \left[\sum_{j=1}^{n} \tau_{1,j} \ldots \sum_{j=1}^{n} \tau_{n,j} \right] \tag{6}$$

and

$$A_p = (1/n) \left[\sum_{j=1}^{n} \tau_{1,j} \cdot a_{1,j} \ldots \sum_{j=1}^{n} \tau_{n,j} \cdot a_{n,j} \right] \tag{7}$$

where T_p and A_p are $1 \times n$ latency projections of the TD and AWTD matrices, respectively. Thus T_p and A_p are row vectors whose elements represent latency and amplitude-weighted latency at each ROI. These projections can be represented in 3D image format (e.g., [Fig. 2]()). Critically, the projection technique is valid only if the TD and AWTD matrices are significantly transitive. Transitivity refers to the existence of consistent lag relations. Perfect transitivity means that the sum of lags over all closed loops is exactly zero. Given measurement error, perfect transitivity is never observed in real neural data. A test for significant transitivity can be implemented by considering all time series triples ([Nikolic 2007]()). Partial transitivity is defined as the fraction of all possible triples in a TD matrix that exhibit transitivity. A TD matrix is said to be significantly transitive if the fraction of all possible triples that exhibit transitivity significantly exceeds the number expected by chance alone ($P < 0.05$). All TD and AWTD matrices presented here satisfy this condition. Additional details regarding the projection technique are given in [Schneider et al. (2006)]().

Latency projections represent spatiotemporal processes in the brain. An estimate of the regional amplitude (in units of BOLD percent change) of each such process can be computed as the quotient of A_p divided by T_p. Thus

$$Amp = A_p./T_p \tag{8}$$

where the division is performed elementwise. Amp is a $1 \times n$ row vector, which we refer to as the latency process amplitude (LPA) image, that estimates the contribution of the spatiotemporal process to the total BOLD time series at each ROI. To compute this estimate, we first apply principal component (PC) analysis (PCA) to the complete set of BOLD time series. PCA assigns a percentage of the variance in the BOLD time series to each PC. Amp is projected onto each PC to find a weight w_i:

$$w_iAmp = Proj(Amp, PC_iBOLD), i = 1 \ldots n \tag{9}$$

These weights are used to compute a weighted sum of PC variances:

$$VarLPBOLD = \sum_i w_iAmp \cdot VarPC_iBOLD, i = 1 \ldots n \tag{10}$$

Thus each latency projection accounts for a computable fraction, Var_{LP}, of BOLD time series variance. Analogously, the TD matrix is subjected to PCA, and latency projections (in units of seconds) are projected onto the TD matrix eigenvectors.

$$wiLP=Proj(LP,PCiTD), i=1 \ldots n \qquad (11)$$

These weights are used to compute the variance of the TD matrix accounted for by the latency projection.

$$VarLPTD=\textstyle\sum_i wiLP \cdot VarPCiTD, i=1 \ldots n \qquad (12)$$

IMAGING METHODS

Participants. Four extant, independent data sets were analyzed in this study. A large data set (n = 692) was obtained from the Harvard-MGH Brain Genomics Superstruct Project (Yeo et al. 2011) (*data set 1*, Table 1). The 692 subjects in *data set 1* were randomly divided into 7 cohorts of ~99 subjects each to test the reproducibility of our analyses. Three additional data sets (Fox et al. 2005b, 2007; Shannon et al. 2013) were previously acquired at the Neuroimaging Laboratories of the Mallinckrodt Institute of Radiology at the Washington University School of Medicine (*data sets 2–4*, see Table 1). All subjects were young adults screened to exclude neurological impairment and psychotropic medications. Demographic information and acquisition parameters are given in Table 1.

MRI acquisition. Imaging was performed with a 3T Siemens Allegra (Washington University) or a 3T Siemens Tim Trio (Harvard-MGH) scanner. Functional images were acquired with a BOLD contrast-sensitive gradient echo echo-planar sequence (parameters listed in Table 1). In *data set 1*, all participants were simply instructed to keep their eyes open, remain still, and not fall asleep. Two fMRI runs were acquired per subject. In *data set 2*, three runs were acquired in the eyes-open visual fixation condition and three runs were acquired with eyes closed (Fox et al. 2005b). In *data set 3*, we contrasted two resting-state runs separately acquired before and after an intervening run during which subjects performed an attention-demanding button-press task (Fox et al. 2007). During the button-press task, subjects were instructed to press a button in response to a visual cue (dimming of the fixation cross hair). In *data set 4*, we contrasted two resting-state runs acquired in the morning (~1 h after each subject's usual wake time) and evening (~2 h before usual bed time). In all data sets, anatomical imaging included one sagittal T1-weighted magnetization prepared rapid gradient echo (MP-RAGE) scan (T1W) and one T2-weighted scan (T2W). The MP-RAGE sequence in *data set 1* was multiecho.

fMRI preprocessing. Initial fMRI preprocessing followed conventional practice (Shulman et al. 2010). Briefly, this included compensation for slice-dependent time shifts, elimination of systematic odd-even slice intensity differences due to interleaved acquisition, and rigid body correction of head movement within and across runs. Atlas transformation was achieved by composition of affine transforms connecting the fMRI volumes with the T2W and T1W structural images. Head movement correction was included with the atlas transformation in a single resampling that gen-

erated volumetric time series in (3 mm)^3 atlas space. Additional preprocessing in preparation for latency analysis included spatial smoothing [6-mm full width at half-maximum (FWHM) Gaussian blur in each direction], voxelwise removal of linear trends over each fMRI run, temporal low-pass filtering retaining frequencies below 0.1 Hz, and zero-meaning each voxel time series. Spurious variance was reduced by regression of nuisance waveforms derived from head motion correction and time series extracted from regions (of "noninterest") in white matter and cerebrospinal fluid (CSF). Nuisance regressors included also the BOLD time series averaged over the brain (Fox et al. 2005b). Additionally, we employed frame-censoring with a threshold of 0.5% root mean square frame-to-frame intensity change (Power et al. 2012). Frame-censoring excluded 3.8 ± 1.1% of all magnetization steady-state frames from the correlation mapping computations.

Gray matter segmentation and ROI definition. All present analyses were restricted to gray matter. A gray matter mask was constructed on the basis of a group-averaged [^{18}F]fluorodeoxyglucose positron emission tomography (FDG-PET) image. Group-level gray matter masks conventionally are constructed by segmenting structural scans, e.g., using FreeSurfer (Fischl 2012). Here we achieved the same objective by thresholding a group average metabolic image, exploiting the fact that gray matter has approximately uniform FDG uptake. This strategy generates smoother gray matter partitions than structural segmentation. The source FDG-PET image, in (3 mm)^3 atlas space, was generated in a separate experiment (Vaishnavi et al. 2010) and was thresholded to exclude white matter, large vessels, and CSF spaces. To reduce the dimensionality of the latency analyses (number of ROIs), the gray matter mask was divided into (6 mm)^3 cubic ROIs, discounting any cubes containing fewer than 50% gray matter voxels.

RESULTS

Resting-state latency projections. Latency projection results obtained in *data set 1* are displayed in Fig. 2. The latency projection result (Fig. 2, A and C) spans ~1 s between the earliest and latest areas of the brain. The principal features of this map are *1*) a high degree of bilateral symmetry and *2*) spatially distinct early and late regions. The earliest and latest brain regions are the posterior cingulate cortex/precuneus (PCC) and the cerebellum, respectively. The amplitude-weighted latency projection (Fig. 2B) and the unweighted TD latency projection (Fig. 2A) exhibit similar topographies. Figure 2D illustrates the across-subgroup spatial correlogram corresponding to the seven subgroups comprising *data set 1*. This correlogram quantitatively demonstrates the spatial similarity between TD and AWTD latency projections (off-diagonal blocks) as well as reproducibility across subgroups (diagonal blocks).

The LPA image (Fig. 3, A and B; see Eq. 8 for derivation) has high values in brain areas that strongly contribute to the brain's latency structure. As is true of the results shown in Fig. 2, the LPA maps are highly similar across subgroups of *data set 1* (Fig. 3C). High-amplitude values appear in the default mode network (DMN) (Raichle et al. 2001), as well as some other areas, most notably the visual cortex. The cerebellum, as a whole, contributes relatively little to the brain's latency structure except in parts that belong to the DMN (Crus II and the inferior vermis). We note that the topographies of lag (Fig. 2, A and C) and LPA (Fig. 3, A and B) are distinct.

The amplitude map can be used to estimate the relative contribution of the corresponding latency projection to the total variance of the BOLD signal within gray matter. This accounting is analogous to fractionating variance by PCA. In our data, on average, 20.1% (±0.7%) of the total variance in the whole brain BOLD signal time series is explained by the latency projection (*Eq. 10*). Moreover, 71.5% (±1.4%) of the TD matrix variance is attributable to the latency projection (*Eq. 12*). Therefore, the latency process we have identified is a significant driver of sequential BOLD activity in the resting state, but it represents only a first component.

State contrasts.   The effect of state contrast on the latency structure of intrinsic activity was studied in three experiments. We first compared the eyes-open versus the eyes-closed condition (EO-EC) (*data set 2*, Table 1). In the eyes-open state, subjects were instructed to maintain visual fixation on a small cross hair. This state contrast is known to modulate the amplitude of intrinsic BOLD activity in visual cortex (Marx et al. 2004; McAvoy et al. 2008). The latency projection correlates of this experiment are shown in Fig. 4. The most prominent change in latency was a shift toward later values in the dorsal visual stream with eyes open compared with eyes closed. Similar changes were observed in the ventral visual stream, curiously omitting V1. The LPA also showed a large shift toward higher values in the dorsal visual stream with eyes closed compared with eyes open. This result is consistent with numerous previous reports documenting reduced amplitude of BOLD fluctuations in the eyes-open state (Bianciardi et al. 2009; Marx et al. 2004; McAvoy et al. 2008). This set of observations is significant in the light of potential relations between latency and perfusion (see below).

In the second experiment, we compared the resting state after versus before performance of a cued right-hand button-press task (Fox et al. 2006, 2007). During the task fMRI run, subjects were instructed to press a button in response to a visual cue (dimming of the fixation cross hair). The most prominent latency change was a shift toward later latency values in left ventral motor cortex following task performance (Fig. 5). A shift toward earlier latency values was observed in bilateral striatum, although this effect was significant in only a small cluster of voxels in the right putamen (Fig. 5*D*). As opposed to the EO-EC experiment, this contrast was computed over two identical resting-state conditions (i.e., before and after task performance) rather than concurrent state contrast (i.e., eyes open at rest vs. eyes closed at rest). Consequently, the change in latency structure seen after the button-press task is a function of antecedent task performance. The LPA showed a large reduction in the PCC (Fig. 5*E*). No LPA change was observed in the voxels showing significant latency shifts. Thus the LPA and latency effects were spatially dissociated in the button-press paradigm, whereas in the EO-EC experiment the effects were spatially overlapping.

Finally, we contrasted resting-state latency in data acquired shortly after waking in the morning and just prior to retiring in the evening (Shannon et al. 2013). This contrast was chosen specifically because it revealed significant diurnal changes in functional connectivity bilaterally in entorhinal cortex (magenta region in Fig. 6*E*). In the morning, entorhinal cortices were functionally connected prominently to anterior insula. In the evening, entorhinal cortices exhibited strong functional connectivity with cortical areas involved in memory retrieval as well as a significant reduction in functional connectivity with anterior insula. The present results, shown in Fig. 6, *A*–*D*, demonstrate significant latency changes in the entorhinal cortices from late in the morning (Fig. 6*A*) to relatively early in the evening (Fig. 6*B*). In contrast, latency shifted in the opposite di-

rection in insular cortex (i.e., later in the evening compared with morning). There were no statistically significant changes in LPA in the morning vs. evening contrast, again demonstrating that latency and amplitude effects can be dissociated.

Latency in relation to RSNs. Inspection of Fig. 2*A* suggests a similarity in spatial scale between RSNs (Fig. 7) and latency maps. This observation raises the question of the relation between RSNs and latency maps. To address this question, we computed the mean latency within each RSN. The obtained result was remarkably close to zero in every RSN (root mean square latency value averaged over RSNs = 0.03 s). This outcome is not imposed by our analytic strategy. We generated surrogate RSNs matched in spatial frequency and scale to true RSNs to test whether the orthogonal relationship between RSNs and latency structure could be attributed to chance (Fig. 7; see APPENDIX for more details). This analysis indicated that the likelihood of observing a root mean square value of 0.03 s is <1% (Fig. 8), suggesting that the observed latency-RSN relationship is not attributable to chance alone. The implication of this result is that no RSN is either early or late. Instead, activity propagates both through and across RSNs.

Figure 9 shows the TD matrix corresponding to the results shown in Fig. 2. Critically, the ROIs have been ordered first by RSN membership (Hacker et al. 2013) (see Fig. 7) and, within RSN, by temporal order using latency projections by RSN block. Figure 9 also includes voxels assigned to the CSF category. The diagonal blocks in the TD matrix represent latency within RSNs (e.g., within DMN latencies, outlined in white); the off-diagonal blocks represent latencies across RSNs.

Figure 9 includes some features that are algebraically constrained. In particular, the TD matrix is anti-symmetric. Therefore, each diagonal block is anti-symmetric as well. However, the algebra does not impose any relation between latency and RSN membership. Therefore, the structure evident in Fig. 9 is informative. The diagonal blocks show a wide range and well-ordered distribution of latencies. Thus activity propagation is present within each RSN. The CSF block is much less well ordered even though it was analyzed identically to the true RSNs. This distinction demonstrates that the observed intra-RSN latency structure reflects brain organization at the systems level and is not an algebraic artifact.

The off-diagonal blocks represent activity propagation across networks. Each block contains well-ordered early, middle, and late components much like the diagonal blocks. Again, this is not algebraically imposed. To obtain a numerical measure of latency spread within blocks, we computed the latency standard deviation. The mean value of this measure across the diagonal blocks was 0.15 s. The same result (0.15 s) was obtained in off-diagonal blocks. The existence of latency ordering within off-diagonal blocks suggests organized lag relations between constituent parts of RSNs. As an example, consider the off-diagonal block corresponding to the DMN paired with the dorsal attention network (DAN), outlined in white in Fig. 9; a well-ordered progression from early (blue) to late (red) is evident, indicating that parts of the DMN lead the DAN and vice versa. Again, a comparison with the CSF blocks is informative. Very little structure is evident in the DAN:CSF block (outlined in white in Fig. 9), reflecting the absence of organized reciprocal latency.

To examine the possibility that the latency process is present with more power within certain RSNs or RSN pairs, we computed the AWTD matrix (Fig. 10), in which ROIs are ordered as in Fig. 9. Since the lag values are weighted by amplitude, ROI interactions with little power have values closer to zero (green hues in Fig. 10). As above, we computed a measure of spread within blocks as the amplitude-weighted latency standard deviation. Among the RSNs, the DMN and visual network (VIS) exhibited the greatest spread of amplitude-weighted latencies. This feature appears in Fig. 10 as a high level of blue/red saturation. In contrast, the CSF blocks are comprised primarily of values near zero (green in Fig. 10). These results are in line with Fig. 3. The critical feature in Fig. 10 is that the diagonal and off-diagonal blocks are comparably saturated. In quantitative terms, the diagonal and off-diagonal blocks exhibit comparable mean standard deviations (0.35 and 0.33, respectively, in units of amplitude·seconds). Combining the results shown in Figs. 9 and 10 implies that lag amplitudes are similarly distributed within and across RSNs.

Control analyses. We considered three nonneuronal explanations for the spatial patterns of BOLD latency projections (Fig. 2). First, is there a relationship to vascular territories (anterior cerebral artery, middle cerebral artery, posterior cerebral artery)? Reference to standard vascular territory maps (Damasio 1983) shows no clear correspondence. In particular, Fig. 2 shows latency contrast around the ventral central sulcus, whereas this part of the brain and widely surrounding areas are all middle cerebral artery territory. Although different vascular territories see arterial blood at different latencies with respect to the aorta, there is no parsimonious mechanism by which this difference could translate to differential BOLD signal latencies. Second, better-perfused tissue may be expected to show a more prompt response to neural activity. In fact, precisely this mechanism probably accounts for delayed BOLD signals in the vicinity of recent infarcts (Amemiya et al. 2014). Accordingly, we compared latency projections to a group average perfusion map constructed on the basis of PET data (Vaishnavi et al. 2010). A scatterplot of cerebral blood flow (CBF) versus latency was constructed (Fig. 11). Inspection of this plot showed no clear evidence of a systematic relation between CBF and latency (Pearson $r = -0.05$). A negative correlation is in line with the theory that better-perfused tissue shows more prompt BOLD response to neuronal activity. However, this effect is negligible, as it only explains 2.5% of latency variance.

Finally, it is well known that the BOLD signal is strongly weighted toward the venous side of the circulation (Hall et al. 2002). Therefore, the BOLD signal in cerebral veins should appear at late latencies (Lee et al. 1995). To investigate this possibility, a group average "venogram" was constructed by computing the voxelwise beta-map corresponding to the differentiated global signal (see APPENDIX for details). Thresholding this map to retain only negative values generated an image demarcating the major venous structures in the head (Fig. 12). Reference to this map demonstrated that cerebral venous structures do account for some features of the latency map, in particular, lateness in the superior and sagittal sinuses. Most of the vascular spaces, however, were already excluded from our analysis by our gray matter mask (see IMAGING METHODS). Thus most of the features evident in Fig. 2 do not correspond to the "venogram" and, therefore, are not attributable to cerebral venous outflow.

DISCUSSION

Summary of present findings. We used latency projections (Nikolic 2007) to study the lag structure of the resting state BOLD signal in healthy young adults. Substantial consistency was demonstrated over seven large cohorts. The amplitude of lagged activity was highest in the default mode, control, and visual networks. LPA estimation indicated that the spatiotemporal process shown in Fig. 2A accounts for ~20% of the resting-state BOLD signal. These results provide a means of studying integration within and across RSNs, which so far have been defined primarily in terms of network segregation.

We studied the effects of three state contrasts (eyes open vs. eyes closed, before vs. after right-handed button press in response to visual cue, morning vs. evening) to test whether latency structure depends on neuronal activity. Temporal structure was modified, with appropriate focality, in all three experiments, suggesting that the latency structure is indeed neuronally driven.

TD matrices (Fig. 9) suggest functional integration within and across RSNs. Surprisingly, we found that the temporal structure of the BOLD signal is orthogonal to RSN topography. In other words, there is equivalent activity propagation both within and across RSNs. The well-ordered organization of activity propagation within and across RSNs contrasts with the highly disorganized activity evident in CSF, demonstrating that the observed propagation structure is not algebraically imposed. By generating surrogate RSNs, we demonstrated that the orthogonal relationship between RSNs and latency is not attributable to chance (Fig. 7, APPENDIX).

Finally, we investigated the effects of CBF and large vascular structures on latency structure. CBF was found to have negligible explanatory power (Fig. 11). The superior sagittal sinus contributed some late features in the latency map, but masking the latency image by an fMRI-derived "venogram" (see APPENDIX) demonstrated that most latency features are not attributable to large vascular structures (Fig. 12).

Observed latency in relation to vascular physiology. The BOLD signal is governed by the local concentration of deoxyhemoglobin, which is paramagnetic and, therefore, an MRI contrast agent (Ogawa et al. 1990). Changes in the fMRI BOLD signal, either task related or spontaneous, reflect changes in blood flow that are greater than changes in oxygen consumption. These changes have been physiologically linked to changes in local field potentials (Goense and Logothetis 2008; Logothetis 2008; Logothetis et al. 2001; Logothetis and Wandell 2004) and cellular metabolism [i.e., changes in cellular redox states (Mintun et al. 2004; Vern et al. 1997, 1998) and aerobic glycolysis (see Raichle and Mintun 2006 for review)]. Most recently, propagated activity in the mouse brain (see *Neurophysiology of latency*) has been visualized with VSD imaging (Mohajerani et al. 2010, 2013), which entirely avoids the question of neurovascular coupling. Nevertheless, concern lingers that regional variations in the latency of neurovascular coupling could largely account for observed delay structure (Friston 2009, 2011; Friston et al. 2013; Friston and Dolan 2010; Handwerker et al. 2004).

Hemodynamic and neuronal contributions to observed lag structure cannot be separated on the basis of the BOLD signal alone. However, we can adjudicate between a primarily neuronal versus primarily hemodynamic explanation for observed lag structure by considering the plausibility of each of these explanations for our results.

First, we find changes in latency structure as a result of state contrasts (Figs. 4–6). A vascular explanation for this result implies focal changes in the dynamics of neurovascular coupling. It might be argued that the latency differences in Figs. 4 and 6 reflect changes in sympathetic tone (due to eye closure or time of day) leading to altered vascular dynamics. However, Fig. 5 contrasts two resting states separated by a task run. It is highly plausible that task performance leaves a neural trace. In fact, such traces must underlie episodic memory and skill acquisition. It is much less plausible, although not inconceivable, that prior task performance leaves a trace manifesting as focally altered vascular hemodynamic coupling. Second, latency projections are orthogonal to RSNs (Figs. 7 and 8) in a manner not attributable to chance. Thus there exists a structured relationship between RSNs, which unquestionably reflect neuronal activity, and latency projections. A purely vascular explanation for this relationship is difficult to imagine, although we cannot exclude it. Conversely, a neuronal explanation for this relationship suggests that lagged activity plays a role in functional integration across segregated brain networks. Third, let us suppose that regional differences in neurovascular coupling delays do exist. We further assume that neural processes are effectively simultaneous, that is, we neglect axonal conduction delays on the order of tens of milliseconds (Vicente et al. 2008). Then, by hypothesis, some regions transduce neural activity into a BOLD signal before other regions. This time shift can be represented as a set of ordered relations, as illustrated in Fig. 2. We show in the APPENDIX that such a structure gives rise to a lag matrix of dimensionality exactly 1. However, Bayesian information criterion analysis (Minka 2001) indicates that the most likely dimensionality of the BOLD TD matrix (Fig. 9) is 2 (Fig. 13, see APPENDIX for details). This result implies the existence of two transitive systems of lags within the TD matrix. Regionally dependent latencies in neurovascular coupling mathematically can account for only one of these (see APPENDIX). Therefore, regionally dependent hemodynamic delays, even if they exist, cannot account for the entirety of the observed latency structure.

Although these considerations argue for a neuronal basis for latency structure, the present fMRI data provide only indirect evidence. Future direct tests combining other modalities (e.g., metabolic or electrophysiological) with fMRI will be necessary to definitely assess the physiological basis of latency structure.

Neurophysiology of latency. Several features in our latency projection results are consistent with previous identification of sources and sinks of intrinsic activity obtained with VAR modeling. Sources and sinks correspond, respectively, to early and late areas in the latency structure. Specifically, Garg and colleagues found that inferior parietal cortex and PCC are sources of propagated activity (Garg et al. 2011). This result matches our assignment of these regions as early in the latency projection (Fig. 2). Similarly, Deshpande and colleagues identified the DMN as a major locus of propagated intrinsic brain activity, in agreement with our amplitude map result (Fig. 3) (Deshpande et al. 2011). Moreover, the anterior prefrontal cortex was reported to be a sink of propagated activity, which matches our assignment of this region as late in the latency projection (Fig. 2). Many of the above-discussed features were also obtained by Majeed and colleagues with a novel iterative technique based on computing lagged correlation functions (Majeed et al. 2011).

Propagated activity is well documented in the electrophysiology literature. Recent work in the mouse using VSD imaging has documented wavelike propagation of both evoked and spontaneous activity (Ferezou et al. 2007; Han et al. 2008; Huang et al. 2010; Mohajerani et al. 2010, 2013; Sato

et al. 2012). Although VSD is capable of millisecond temporal resolution, the observed spontaneous activity motifs in the mouse cortex play out over ~0.5 s (Mohajerani et al. 2010, 2013), in close agreement with our results (Fig. 2*A*). The speed of spontaneous activity propagation in the mouse has been estimated as ~0.2 m/s (Han et al. 2008; Mohajerani et al. 2010). In our data, we take as typical a latency difference of 0.5 s over 10 cm, which yields a propagation speed of 0.2 m/s, in agreement with the mouse estimate. Slow wave propagation has also been documented during slow wave sleep (SWS). The speed of slow wave propagation in SWS has been estimated as 0.4–6.3 m/s (Massimini et al. 2004; Murphy et al. 2009b). This speed of propagation estimate is reasonably comparable to the estimate from our data (0.2 m/s, see above), given that the SWS figure was obtained on the basis of scalp electroencephalography (EEG) and inverse source modeling (Murphy et al. 2009b). Interestingly, Murphy and colleagues report that the DMN is preferentially involved in slow wave propagation during SWS (Murphy et al. 2009b), which is concordant with our finding that the DMN is represented with high amplitude in the latency projection (Fig. 3). Although SWS and waking quiet rest are distinct states, intrinsic activity exhibits many similarities across levels of arousal (Larson-Prior et al. 2009; Vincent et al. 2007). RSNs are present, albeit with arousal-dependent features, in both wakefulness and SWS (Samann et al. 2011). Substantial evidence indicates that the slow waves in SWS represent UP and DOWN state oscillations (Huber et al. 2004; Massimini et al. 2004; Murphy et al. 2009b; Yuste 1997). It has been reported that UP and DOWN states persist during wakefulness, although they are intermixed with other activity and are much less periodic (Vyazovskiy et al. 2011). If so, the same mechanism may drive slow activity in waking and SWS. Thus there exists a plausible electrophysiological mechanism underlying slow propagated BOLD activity.

Murphy and colleagues find that sources and sinks of spontaneous activity in the mouse recapitulate patterns of activity observed in task responses (Mohajerani et al. 2013). In other words, primary areas (such as primary somatosensory cortex) tend to be sources in task-evoked and spontaneous activity, while higher-order areas such as the parietal lobule are sinks during task-evoked and spontaneous activity. Our results show partial correspondence with this principle. In particular, primary motor cortex is early and superior parietal lobule is late (Fig. 2*C*), in agreement with task-evoked studies in mice (Mohajerani et al. 2013). Additionally, lateral prefrontal cortex exhibits very delayed response to item recognition trials (Schacter et al. 1997), which is in agreement with our spontaneous activity lag results (Fig. 2, *A* and *C*). However, primary sensory and auditory cortices are late in our data (Fig. 2*C*), in contrast with the Murphy results. These divergences could be attributable to differences in species or technique, but we believe that the more likely explanation lies in a fundamental distinction between spontaneous and task-evoked activity. Task-evoked BOLD responses in humans exhibit a wide variety of waveforms and variable mixtures of sustained and transient components, depending on locus and task paradigm (Fox et al. 2005a; Gonzalez-Castillo et al. 2012). Moreover, these responses play out on a timescale on the order of several seconds. In contrast, our lag results are generally confined to a range of ±0.5 s. Thus, although there may be some shared motifs between lagged spontaneous and task-evoked activity, the two phenomena most likely represent different processes with different temporal structures (see Raichle 2011 for further discussion).

Functional significance of latency. It is striking that the resting-state BOLD signal, which has been used to identify spatially segregated functional networks (Power et al. 2011; Yeo et al. 2011), also carries a signature of functional integration within and across RSNs. Critically, resting-state activity propagation is directed, as reflected in a latency map (Fig. 2). Thus there is a stereotyped pattern of activity propagation in the human brain, such that, on average, certain brain loci initiate propagated activity (early regions) while other loci are destinations (late regions). While it is widely believed that cross-network communication underlies brain function (Bressler and Menon 2010), discussion of this point largely derives from task-based experiments. Our analyses reveal loci corresponding to sources and sinks of propagated intrinsic activity. Remarkably, many of the same loci have been independently identified, on the basis of task-based fMRI, as key cortical nodes regulating behavior (Bressler and Menon 2010; Nelson et al. 2010). Specifically, these loci (Fig. 2C) are PCC (early), ventromedial prefrontal cortex (VMPFC, late), dorsal anterior cingulate cortex (dACC, early), anterior insula (AI, late), posterior parietal cortex (PPC, early), and dorsolateral prefrontal cortex (DLPFC, late). These areas represent three pairs of regions belonging to the default mode, salience, and fronto-parietal control networks, respectively. It is probably not coincidental that, within each network pair, one region is early while the other is late. Indeed, the orthogonality of RSN and latency topography suggests that propagated activity in the resting state may serve as a framework for RSN integration. Thus analyzing latency structure might be a useful method to increase our understanding of cognitive processes, whether they are physiological or pathological in nature.

One feature of our results that deserves further comment is that the cerebellum as a whole is late in the latency map (Fig. 2A). The cerebellum is widely regarded as responsible for reflexive adjustments during active behavior (Buckner et al. 2011; Leiner et al. 1991; Strick et al. 2009), for example, adjusting motor programs in response to unanticipated changes in environmental parameters (e.g., load). In the resting state, the role of the cerebellum appears to be minor, as reflected by the low amplitude of intrinsic cerebellar BOLD fluctuations (Li et al. 2012; Logothetis and Wandell 2004). Our data suggest that, at least in the resting state, the primary direction of information flow appears to be from prosencephalon to cerebellum. This observation is consistent with the current understanding of the cerebellum as primarily a receiver of multimodal information from the cerebral cortex (Leiner et al. 1991). Nonetheless, we cannot exclude the possibility that the vascular response to neural demand is generally late in the cerebellum. However, this explanation would be specific to the cerebellum as opposed to the posterior circulation, because visual and infero-temporal cortices are mostly early.

State contrasts in latency. The original motivation for examining state contrasts was to present evidence that neuronal phenomenology drives latency structure. However, the observed effects of state contrast on latency are potentially of physiological interest. In the eyes-open condition, propagated signals appear to flow from primary to higher-order visual cortex (Fig. 4A), in accordance with known direction information flow in visual processing (Van Essen et al. 1992). In the eyes-closed condition, the direction of signal propagation appears to reverse (Fig. 4B). Speculatively, this reversal may reflect may reflect top-down influences supporting mental imagery (Stokes et al. 2009). In the button-press contrast, we theorize that changes in latency after performance of a motor task reflect physiological processes related to learning. Although the task is simple (pressing a button in response to cross-hair dimming), it is attention demanding, and subjects do show

an improvement in reaction time (data not shown). Enhanced signaling from putamen to the left motor region (Fig. 5D) may underlie this improvement. This result is consistent for the known role of the putamen in motor learning (Grafton et al. 1995).

The presently observed latency differences between morning and evening (Fig. 6, C and D) spatially correspond to previously reported functional connectivity changes in medial temporal lobe and insula (Fig. 6E; Shannon et al. 2013). The previous findings point to changes in signal correlation; the present results point to diurnal changes in directed signaling. Specifically, the entorhinal cortex is late in the morning and early in the evening. Entorhinal cortex is the main interface between hippocampus and neocortex (Lavenex and Amaral 2000). It is believed that the hippocampus accumulates encoded experiences during the day and that this form of memory is labile (Axmacher et al. 2009). Memory consolidation is thought to require transfer of information from hippocampus to neocortex, which takes place later in the day and during sleep (Axmacher et al. 2009). Accordingly, entorhinal cortex may be late in the morning because it is acting as an information accumulator. Conversely, entorhinal cortex is early in the evening because it is transferring information to cortex, thereby facilitating formation of hippocampal independent memories. The insula is relatively early in the morning and late in the evening. Interpreting this effect will require further investigation.

Limitations. There are three principal limitations of this work. First, our method for estimating latencies (parabolic interpolation of pairwise cross-covariance estimates) undoubtedly includes some imprecision, in part because the temporal sampling density is relatively low (see repetition times in Table 1). However, our conclusions are based on results obtained at the group level. These group-level latency estimates are reproducible across seven large cohorts (Fig. 2D).

Second, our findings are based on resting-state fMRI data preprocessed with global signal regression (GSR). GSR is a controversial processing step (Fox et al. 2009; Murphy et al. 2009a); however, in preliminary analyses, it was determined that omission of GSR greatly reduces the range of observed latencies. This is easily understandable as a consequence of retaining large quantities of instantaneously correlated shared variance. It is likely that some fraction of the global signal is neuronally derived (Scholvinck et al. 2010); however, it is certain that a large fraction is nonneuronal artifact attributable to head motion (Power et al. 2012, 2013; Yan et al. 2013) and variable P_{CO_2} (Birn et al. 2006). Moreover, the artifactual component of the global signal exhibits substantial cross-subject variability (He and Liu 2012; Power et al. 2013). Therefore, GSR is a necessary noise-reduction technique in the present analysis.

Finally, to estimate the statistical significance of the orthogonality of latency structure with respect to RSNs, we developed a method to generate surrogate RSNs with the aim of matching the spatial characteristics of real RSNs (see APPENDIX). While the topology of true RSN structure was preserved in the surrogates, the spatial frequency distribution was only approximately matched (Fig. 7). Nevertheless, we are persuaded that the orthogonality relationship is statistically significant.

GRANTS

DISCLOSURES

No conflicts of interest, financial or otherwise, are declared by the author(s).

AUTHOR CONTRIBUTIONS

Author contributions: A.M., A.Z.S., and M.E.R. conception and design of research; A.M. analyzed data; A.M., A.Z.S., and M.E.R. interpreted results of experiments; A.M. and C.D.H. prepared figures; A.M. drafted manuscript; A.M., A.Z.S., and M.E.R. edited and revised manuscript; A.M., A.Z.S., C.D.H., and M.E.R. approved final version of manuscript.

ACKNOWLEDGMENTS

Appendix

Alternative Strategies for Computing and Analyzing Latencies We directly computed lags between time series on the basis of lagged cross-covariance functions. Parabolic interpolation was used to determine the lag of maximal covariance at a temporal resolution finer than the sampling density. An alternative method based on iterating lagged correlation functions has been described (Majeed et al. 2009, 2011), but it applies to whole images as opposed to ROI pairs. Additionally, the iterative method provides no basis for calculating what percentage of variance is attributable to latency components. The major alternative strategy for estimating lags is the phase-slope method, in which lag is computed as the derivative with respect to frequency of complex coherence phase (Jenkins and Watts 1968). Although the phase-slope method has been used to analyze fMRI data (Hinkley et al. 2013; Sun et al. 2005), we chose a time domain method because the frequency domain method requires differentiation, which yields noisy and unstable estimates. Moreover, the phase-slope method requires evaluating slope over some interval under the assumption that the slope is constant, which is not necessarily true.

Having obtained a TD matrix by any method, alternatives for extracting latency components include the present (projection) method (Nikolic 2007; Schneider et al. 2006) and eigenvector decomposition. We tested both approaches and found that the principal eigenvector generally is very similar to the result obtained by the projection method. However, the projection method yielded much more reproducible results in the cross-subgroup analysis shown in Fig. 2.

A substantial body of previous work has applied VAR methods to the study of directed influences in fMRI data ([Deshpande et al. 2011](); [Friston et al. 2003](); [Garg et al. 2011](); [Goebel et al. 2003](); [Smith et al. 2012]()). All of these methods require the computation of $k \times k \times \tau$ matrices, where k is the number of ROIs and τ is the order of the model. Even if model order is limited to 1 ([Garg et al. 2011](); [Smith et al. 2012]()), VAR does not directly return lag, which is the present quantity of interest. Dynamic causal modeling (dcm) is a VAR-based method for estimating the most likely topology of directed graphs. However, in practice, dcm is limited to a handful of ROIs and, therefore, is unsuited to the present investigation. Granger causality ([Deshpande et al. 2011](); [Goebel et al. 2003]()) is theoretically less computationally demanding than dcm but, like dcm, is essentially an information-theoretic analysis. The scope of our analysis is much more restricted and does not rely on models. Our results carry implications regarding the existence of propagated disturbances and directed influences in intrinsic brain activity, but we here avoid information-theoretic approaches in favor of a more concrete and interpretable analysis based on lags.

Generation of surrogate RSNs. We generated surrogate RSNs topologically matched to real RSNs and approximately matched in spatial frequency distribution ([Fig. 7]()). Surrogate RSNs were generated by treating the left hemisphere of the real RSN brain as an element of a high-dimensional symmetric group that respects the topology of the true RSNs. We then applied randomly generated full-rank permutations on the unihemispheric RSN brain partition. In greater detail, the 3D MLP RSN partition was converted to a 1D vector and the ends were connected to form a ring. The ring then was randomly rotated and the 3D to 1D transform inverted. In principle, other group operations could have been applied, but rotation theoretically preserves spatial scale. The resulting 3D map was reflected across the midsagittal line to generate hemispherically symmetric surrogate RSNs. Equivalence of spatial scale was verified by 3D-Fourier analysis ([Fig. 7]()).

Generation of "venograms." Regression frequently is used to compute the topography within the brain of reference signals, e.g., estimated response waveforms in task fMRI. Similarly, the topography of a time-shifted reference signal can be computed by regressing the derivative of the time signal ([Friston et al. 1998]()). This technique is easily understood as an application of a Taylor expansion: f(t+Δt)=f(t)+Δt·dfdt. In the present work, $f(t)$ is the global signal, which has already been removed by regression during preprocessing. Thus regression of the differentiated global signal yields the topography of the delayed global signal, i.e., large venous structures.

Estimation of TD matrix dimensionality. Experimentally observed lag structures include measurement errors. Hence, the dimensionality of our TD matrices must be estimated. To perform this estimation, we ran the procedure created by T. P. Minka, which compares the eigenspectrum of the actual data to the eigenspectrum of a random matrix and expresses the result in terms of likelihood ([Minka 2001]()). The Minka algorithm requires a positive definite matrix. As the TD matrix is not positive definite, the algorithm was run on the square of the TD matrix, which is mathematically required to have the same dimensionality as the TD matrix itself ([Allison et al. 2010]()). The most likely dimensionality of the lag structure illustrated in [Fig. 9]() is 2 ([Fig. 13]()).

Dimensionality of a TD matrix representing a single set of fixed delays. We prove that a fixed set of regionally distinct neurovascular coupling delays explains only one component of a TD matrix. The proof depends on showing that a TD matrix representing a single set of lagged relationships has

only a single eigenvector.

Let the fixed set of regional delays be represented as the column vector, $(d_1 d_2 d_3 \vdots d_n)$, where n is the number of regions. Suppose that T is the anti-symmetric matrix generated by this set of delays. Thus

$$T = [0 \ldots \tau_{1,n} \vdots \ddots \vdots -\tau_{1,n} \cdots 0] = [0 \ldots d_n - d_1 \vdots \ddots \vdots d_1 - d_n \ldots 0] \tag{A1}$$

Previous work has shown that, for a nonzero anti-symmetric matrix $A \in \mathbb{R}^{n \times n}$, $rank(A) \leq 2k$ if and only if there exists $\boldsymbol{x}_1, \ldots, \boldsymbol{x}_k, \boldsymbol{y}_1, \ldots \boldsymbol{y}_1 \in \mathbb{R}^n$ such that $A = \sum_{i=1}^k (x_i y_i^T - y_i x_i^T)$ ([Allison et al. 2010](#)). Hence, if we construct $\boldsymbol{x}, \boldsymbol{y}$ such that $T = \boldsymbol{x}\boldsymbol{y}^T - \boldsymbol{y}\boldsymbol{x}^T$, then $k = 1$, and $rank(T) \leq 2$. Since the rank of any anti-symmetric matrix over $\mathbb{R}$ must be even ([Allison et al. 2010](#)), $rank(T) = 2$, as T is nonzero. The eigenvalues of a real, anti-symmetric matrix come in conjugate imaginary pairs ([Allison et al. 2010](#)). Therefore, T has only two conjugate imaginary eigenvalues, $\pm ci$, corresponding to a single eigenvector, $\pm v$, except for sign. Note that the dimensionality of T is 1 even though its rank is 2. This is because for all real, anti-symmetric matrices, the rank is 2 times the dimensionality, as eigenvalues come in conjugate imaginary pairs (see above). Thus, once we construct $\boldsymbol{x}, \boldsymbol{y}$ such that $T = \boldsymbol{x}\boldsymbol{y}^T - \boldsymbol{y}\boldsymbol{x}^T$, we have proven that a TD matrix representing a single set of lagged relationships has only a single eigenvector.

Now, it remains to construct $\boldsymbol{x}, \boldsymbol{y}$ such that $T = \boldsymbol{x}\boldsymbol{y}^T - \boldsymbol{y}\boldsymbol{x}^T$. Let $\boldsymbol{x} \in \mathbb{R}^n$ such that $x_i = 1$ for all x and $y_j = d_j$ for $j = i, \ldots, n$. Then

$$\boldsymbol{xy}^T - \boldsymbol{yx}^T = \begin{pmatrix} 1 \\ 1 \\ 1 \\ \cdot \\ \cdot \\ \cdot \\ 1 \end{pmatrix} (d_1 \; d_2 \ldots d_n) - \begin{pmatrix} d_1 \\ d_2 \\ d_3 \\ \cdot \\ \cdot \\ \cdot \\ d_n \end{pmatrix} (1 \quad 1 \quad 1 \quad \ldots \quad 1)$$

$$= \begin{bmatrix} d_1 \, d_2 & \ldots & d_n \\ d_1 \, d_2 & \ldots & d_n \\ & \cdot & \\ & \cdot & \\ & \cdot & \\ d_1 \, d_2 & \ldots & d_n \end{bmatrix} - \begin{bmatrix} d_1 \, d_1 & \ldots & d_1 \\ d_2 \, d_2 & \ldots & d_2 \\ & \cdot & \\ & \cdot & \\ & \cdot & \\ d_n \, d_n & \ldots & d_n \end{bmatrix} \qquad (A2)$$

$$= \begin{bmatrix} 0 & \ldots & d_n - d_1 \\ \vdots & \ddots & \vdots \\ d_1 - d_n & \ldots & 0 \end{bmatrix}$$

$$= T$$

completing the construction required for the proof.

An alternative formulation applies the principle that the eigenvalues of a linear system satisfy the characteristic equation of its matrix. We illustrate this principle in a simple case of a 3 × 3 time delay matrix. Let (d1d2d3) be the onset times for the system. Then

$$T = [0 \; d1 - d2 \; d3 - d1 \; d2 - d1 \; 0 \; d2 - d3 \; d3 - d1 \; d3 - d2 \; 0]. \tag{A3}$$

The characteristic equation is

$$det \begin{bmatrix} -\lambda & d_1 - d_2 & d_1 - d_3 \\ d_2 - d_1 & -\lambda & d_2 - d_3 \\ d_3 - d_1 & d_3 - d_2 & -\lambda \end{bmatrix}$$

$$= -\lambda \cdot det \begin{bmatrix} -\lambda & d_2 - d_3 \\ d_3 - d_2 & -\lambda \end{bmatrix} - (d_1 - d_2) det \begin{bmatrix} d_2 - d_1 & d_2 - d_3 \\ d_3 - d_1 & -\lambda \end{bmatrix}$$

$$+ (d_1 - d_3) det \begin{bmatrix} d_2 - d1 & -\lambda \\ d_3 - d_1 & d_3 - d_2 \end{bmatrix} \qquad (A4)$$

$$= -\lambda(\lambda^2 - (d_2 - d_3)(d_3 - d_2)) - (d_1 - d_2)(-\lambda(d_2 - d_1)$$

$$- (d_2 - d_3)(d_3 - d_1)) + (d_1 - d_3)(\lambda(d_3 - d_1) - (d_2 - d_1)(d_3 - d_2))$$

$$= [-\lambda^3 - \lambda(d_2 - d_3)^2] + [-\lambda(d_2 - d_1)^2 + (d_1 - d_2)(d_2 - d_3)$$

$$(d_3 - d_1)] + [-(d_1 - d_2)(d_2 - d_3)(d_3 - d_1) - \lambda((d_3 - d_1)^2]$$

$$= -\lambda^3 - \lambda \sum_{j \neq k} (d_j - d_k)^2 = 0$$

$$\Leftrightarrow \lambda^2 + \sum_{j \neq k} (d_j - d_k)^2 = 0$$

Since $\sum_{j \neq k}(d_j - d_k)^2$ is a sum of squares, it must be positive. Therefore _Eq. A4_ has two conjugate imaginary solutions corresponding to a single eigenvector, as claimed.

REFERENCES

Allison M, Bodine E, DeAlba LM, Debnath J, DeLoss L, Garnett C, Grout J, Hogben L, Im B, Kim H, Nair R, Pryporova O, Savage K, Shader B, Wehe AW. Minimum rank of skew-symmetric matrices described by a graph. _Linear Algebra Appl_ 432: 2457–2472, 2010

Amemiya S, Kunimatsu A, Saito N, Ohtomo K. Cerebral hemodynamic impairment: assessment with resting-state functional MR imaging. _Radiology_ 270: 548–555, 2014 [PubMed: 24072777]

Axmacher N, Draguhn A, Elger CE, Fell J. Memory processes during sleep: beyond the standard consolidation theory. _Cell Mol Life Sci_ 66: 2285–2297, 2009 [PubMed: 19322518]

Beckmann CF, DeLuca M, Devlin JT, Smith SM. Investigations into resting-state connectivity using independent component analysis. _Philos Trans R Soc Lond B Biol Sci_ 360: 1001–1013, 2005 [PMCID: PMC1854918] [PubMed: 16087444]

Bianciardi M, Fukunaga M, van Gelderen P, Horovitz SG, de Zwart JA, Duyn JH. Modulation of spontaneous fMRI activity in human visual cortex by behavioral state. _Neuroimage_ 45: 160–168, 2009 [PMCID: PMC2704889] [PubMed: 19028588]

Birn RM, Diamond JB, Smith MA, Bandettini PA. Separating respiratory-variation-related fluctuations from neuronal-activity-related fluctuations in fMRI. _Neuroimage_ 31: 1536–1548, 2006 [PubMed: 16632379]

Biswal BB, Mennes M, Zuo XN, Gohel S, Kelly C, Smith SM, Beckmann CF, Adelstein JS, Buckner RL, Colcombe S, Dogonowski AM, Ernst M, Fair D, Hampson M, Hoptman MJ, Hyde JS, Kiviniemi VJ, Kotter R, Li SJ, Lin CP, Lowe MJ, Mackay C, Madden DJ, Madsen KH, Margulies DS, Mayberg HS, McMahon K, Monk CS, Mostofsky SH, Nagel BJ, Pekar JJ, Peltier SJ, Petersen SE, Riedl V, Rombouts SA, Rypma B, Schlaggar BL, Schmidt S, Seidler RD, Siegle GJ, Sorg C, Teng GJ, Veijola J, Villringer A, Walter M, Wang L, Weng XC, Whitfield-Gabrieli S, Williamson P, Windischberger C, Zang YF, Zhang HY, Castellanos FX, Milham MP. Toward discovery science of human brain function. *Proc Natl Acad Sci USA* 107: 4734–4739, 2010 [PMCID: PMC2842060] [PubMed: 20176931]

Biswal B, Yetkin FZ, Haughton VM, Hyde JS. Functional connectivity in the motor cortex of resting human brain using echo-planar MRI. *Magn Reson Med* 34: 537–541, 1995 [PubMed: 8524021]

Bressler SL, Menon V. Large-scale brain networks in cognition: emerging methods and principles. *Trends Cogn Sci* 14: 277–290, 2010 [PubMed: 20493761]

Buckner RL, Krienen FM, Castellanos A, Diaz JC, Yeo BT. The organization of the human cerebellum estimated by intrinsic functional connectivity. *J Neurophysiol* 106: 2322–2345, 2011 [PMCID: PMC3214121] [PubMed: 21795627]

Choi EY, Yeo BT, Buckner RL. The organization of the human striatum estimated by intrinsic functional connectivity. *J Neurophysiol* 108: 2242–2263, 2012 [PMCID: PMC3545026] [PubMed: 22832566]

Cordes D, Haughton VM, Arfanakis K, Wendt GJ, Turski PA, Moritz CH, Quigley MA, Meyerand ME. Mapping functionally related regions of brain with functional connectivity MR imaging. *Am J Neuroradiol* 21: 1636–1644, 2000 [PMCID: PMC8174861] [PubMed: 11039342]

Damasio H. A computed tomographic guide to the identification of cerebral vascular territories. *Arch Neurol* 40: 138–142, 1983 [PubMed: 6830451]

Deshpande G, Santhanam P, Hu X. Instantaneous and causal connectivity in resting state brain networks derived from functional MRI data. *Neuroimage* 54: 1043–1052, 2011 [PMCID: PMC2997120] [PubMed: 20850549]

Ferezou I, Haiss F, Gentet LJ, Aronoff R, Weber B, Petersen CC. Spatiotemporal dynamics of cortical sensorimotor integration in behaving mice. *Neuron* 56: 907–923, 2007 [PubMed: 18054865]

Fischl B. FreeSurfer. *Neuroimage* 62: 774–781, 2012 [PMCID: PMC3685476] [PubMed: 22248573]

Fox MD, Greicius M. Clinical applications of resting state functional connectivity. *Front Syst Neurosci* 4: 19, 2010 [PMCID: PMC2893721] [PubMed: 20592951]

Fox MD, Raichle ME. Spontaneous fluctuations in brain activity observed with functional magnetic resonance imaging. *Nat Rev Neurosci* 8: 700–711, 2007 [PubMed: 17704812]

Fox MD, Snyder AZ, Barch DM, Gusnard DA, Raichle ME. Transient BOLD responses at block transitions. *Neuroimage* 28: 956–966, 2005a [PubMed: 16043368]

Fox MD, Snyder AZ, Vincent JL, Corbetta M, Van Essen DC, Raichle ME. The human brain is intrinsically organized into dynamic, anticorrelated functional networks. *Proc Natl Acad Sci USA* 102: 9673–9678, 2005b [PMCID: PMC1157105] [PubMed: 15976020]

Fox MD, Snyder AZ, Vincent JL, Raichle ME. Intrinsic fluctuations within cortical systems account for intertrial variability in human behavior. *Neuron* 56: 171–184, 2007 [PubMed: 17920023]

Fox MD, Snyder AZ, Zacks JM, Raichle ME. Coherent spontaneous activity accounts for trial-to-trial variability in human evoked brain responses. *Nat Neurosci* 9: 23–25, 2006 [PubMed: 16341210]

Fox MD, Zhang D, Snyder AZ, Raichle ME. The global signal and observed anticorrelated resting state brain networks. *J Neurophysiol* 101: 3270–3283, 2009 [PMCID: PMC2694109] [PubMed: 19339462]

Friston K. Causal modelling and brain connectivity in functional magnetic resonance imaging. *PLoS Biol* 7: e33, 2009 [PMCID: PMC2642881] [PubMed: 19226186]

Friston K. Dynamic causal modeling and Granger causality. Comments on: The identification of interacting networks in the brain using fMRI: model selection, causality and deconvolution. *Neuroimage* 58: 303–305, 2011 [PMCID: PMC3183826] [PubMed: 19770049]

Friston K, Moran R, Seth AK. Analysing connectivity with Granger causality and dynamic causal modelling. *Curr Opin Neurobiol* 23: 172–178, 2013 [PMCID: PMC3925802] [PubMed: 23265964]

Friston KJ, Dolan RJ. Computational and dynamic models in neuroimaging. *Neuroimage* 52: 752–765, 2010 [PMCID: PMC2910283] [PubMed: 20036335]

Friston KJ, Fletcher P, Josephs O, Holmes A, Rugg MD, Turner R. Event-related fMRI: characterizing differential responses. *Neuroimage* 7: 30–40, 1998 [PubMed: 9500830]

Friston KJ, Harrison L, Penny W. Dynamic causal modelling. *Neuroimage* 19: 1273–1302, 2003 [PubMed: 12948688]

Garg R, Cecchi GA, Rao AR. Full-brain auto-regressive modeling (FARM) using fMRI. *Neuroimage* 58: 416–441, 2011 [PubMed: 21439388]

Goebel R, Roebroeck A, Kim DS, Formisano E. Investigating directed cortical interactions in time-resolved fMRI data using vector autoregressive modeling and Granger causality mapping. *Magn Reson Imaging* 21: 1251–1261, 2003 [PubMed: 14725933]

Goense JB, Logothetis NK. Neurophysiology of the BOLD fMRI signal in awake monkeys. *Curr Biol* 18: 631–640, 2008 [PubMed: 18439825]

Gonzalez-Castillo J, Saad ZS, Handwerker DA, Inati SJ, Brenowitz N, Bandettini PA. Whole-brain, time-locked activation with simple tasks revealed using massive averaging and model-free analysis. *Proc Natl Acad Sci USA* 109: 5487–5492, 2012 [PMCID: PMC3325687] [PubMed: 22431587]

Grafton ST, Hazeltine E, Ivry R. Functional mapping of sequence learning in normal humans. *J Cogn Neurosci* 7: 497–510, 1995 [PubMed: 23961907]

Hacker CD, Laumann TO, Szrama NP, Baldassarre A, Snyder AZ, Leuthardt EC, Corbetta M. Resting state network estimation in individual subjects. *Neuroimage* 82C: 616–633, 2013 [PMCID: PMC3909699] [PubMed: 23735260]

Hall DA, Goncalves MS, Smith S, Jezzard P, Haggard MP, Kornak J. A method for determining venous contribution to BOLD contrast sensory activation. *Magn Reson Imaging* 20: 695–706, 2002 [PubMed: 12591565]

Han F, Caporale N, Dan Y. Reverberation of recent visual experience in spontaneous cortical waves. *Neuron* 60: 321–327, 2008 [PMCID: PMC3576032] [PubMed: 18957223]

Handwerker DA, Ollinger JM, D'Esposito M. Variation of BOLD hemodynamic responses across subjects and brain regions and their effects on statistical analyses. *Neuroimage* 21: 1639–1651, 2004 [PubMed: 15050587]

He BJ, Zempel JM, Snyder AZ, Raichle ME. The temporal structures and functional significance of scale-free brain activity. *Neuron* 66: 353–369, 2010 [PMCID: PMC2878725] [PubMed: 20471349]

He H, Liu TT. A geometric view of global signal confounds in resting-state functional MRI. *Neuroimage* 59: 2339–2348, 2012 [PMCID: PMC3254803] [PubMed: 21982929]

Hinkley LB, Sekihara K, Owen JP, Westlake KP, Byl NN, Nagarajan SS. Complex-value coherence mapping reveals novel abnormal resting-state functional connectivity networks in task-specific focal hand dystonia. *Front Neurol* 4: 149, 2013 [PMCID: PMC3794296] [PubMed: 24133480]

Huang X, Xu W, Liang J, Takagaki K, Gao X, Wu JY. Spiral wave dynamics in neocortex. *Neuron* 68: 978–990, 2010 [PMCID: PMC4433058] [PubMed: 21145009]

Huber R, Ghilardi MF, Massimini M, Tononi G. Local sleep and learning. *Nature* 430: 78–81, 2004 [PubMed: 15184907]

Jenkins GM, Watts DG. *Spectral Analysis and Its Applications*. San Francisco, CA: Holden-Day, 1968

Konig P. A method for the quantification of synchrony and oscillatory properties of neuronal activity. *J Neurosci Methods* 54: 31–37, 1994 [PubMed: 7815817]

Larson-Prior LJ, Zempel JM, Nolan TS, Prior FW, Snyder AZ, Raichle ME. Cortical network functional connectivity in the descent to sleep. *Proc Natl Acad Sci USA* 106: 4489–4494, 2009 [PMCID: PMC2657465] [PubMed: 19255447]

Lavenex P, Amaral DG. Hippocampal-neocortical interaction: a hierarchy of associativity. *Hippocampus* 10: 420–430, 2000 [PubMed: 10985281]

Lee AT, Glover GH, Meyer CH. Discrimination of large venous vessels in time-course spiral blood-oxygen-level-dependent magnetic-resonance functional neuroimaging. *Magn Reson Med* 33: 745–754, 1995 [PubMed: 7651109]

Leiner HC, Leiner AL, Dow RS. The human cerebro-cerebellar system: its computing, cognitive, and language skills. *Behav Brain Res* 44: 113–128, 1991 [PubMed: 1751002]

Li Z, Zhu Y, Childress AR, Detre JA, Wang Z. Relations between BOLD fMRI-derived resting brain activity and cerebral blood flow. *PLoS One* 7: e44556, 2012 [PMCID: PMC3448607] [PubMed: 23028560]

Logothetis NK. What we can do and what we cannot do with fMRI. *Nature* 453: 869–878, 2008 [PubMed: 18548064]

Logothetis NK, Pauls J, Augath M, Trinath T, Oeltermann A. Neurophysiological investigation of the basis of the fMRI signal. *Nature* 412: 150–157, 2001 [PubMed: 11449264]

Logothetis NK, Wandell BA. Interpreting the BOLD signal. *Annu Rev Physiol* 66: 735–769, 2004 [PubMed: 14977420]

Majeed W, Magnuson M, Hasenkamp W, Schwarb H, Schumacher EH, Barsalou L, Keilholz SD. Spatiotemporal dynamics of low frequency BOLD fluctuations in rats and humans. *Neuroimage* 54: 1140–1150, 2011 [PMCID: PMC2997178] [PubMed: 20728554]

Majeed W, Magnuson M, Keilholz SD. Spatiotemporal dynamics of low frequency fluctuations in BOLD fMRI of the rat. *J Magn Reson Imaging* 30: 384–393, 2009 [PMCID: PMC2758521] [PubMed: 19629982]

Marx E, Deutschlander A, Stephan T, Dieterich M, Wiesmann M, Brandt T. Eyes open and eyes closed as rest conditions: impact on brain activation patterns. *Neuroimage* 21: 1818–1824, 2004 [PubMed: 15050602]

Massimini M, Huber R, Ferrarelli F, Hill S, Tononi G. The sleep slow oscillation as a traveling wave. *J Neurosci* 24: 6862–6870, 2004 [PMCID: PMC6729597] [PubMed: 15295020]

Maxim V, Sendur L, Fadili J, Suckling J, Gould R, Howard R, Bullmore E. Fractional Gaussian noise, functional MRI and Alzheimer's disease. *Neuroimage* 25: 141–158, 2005 [PubMed: 15734351]

McAvoy M, Larson-Prior L, Nolan TS, Vaishnavi SN, Raichle ME, d'Avossa G. Resting states affect spontaneous BOLD oscillations in sensory and paralimbic cortex. *J Neurophysiol* 100: 922–931, 2008 [PMCID: PMC2525732] [PubMed: 18509068]

Minka TP. Automatic choice of dimensionality for PCA. In: *Advances in Neural Information Processing Systems 13*. Cambridge, MA: MIT Press, 2001, p. 598–604

Mintun MA, Vlassenko AG, Rundle MM, Raichle ME. Increased lactate/pyruvate ratio augments blood flow in physiologically activated human brain. *Proc Natl Acad Sci USA* 101: 659–664, 2004 [PMCID: PMC327204] [PubMed: 14704276]

Mohajerani MH, Chan AW, Mohsenvand M, Ledue J, Liu R, McVea DA, Boyd JD, Wang YT, Reimers M, Murphy TH. Spontaneous cortical activity alternates between motifs defined by regional axonal projections. *Nat Neurosci* 16: 1426–1435, 2013 [PMCID: PMC3928052] [PubMed: 23974708]

Mohajerani MH, McVea DA, Fingas M, Murphy TH. Mirrored bilateral slow-wave cortical activity within local circuits revealed by fast bihemispheric voltage-sensitive dye imaging in anesthetized and awake mice. *J Neurosci* 30: 3745–3751, 2010 [PMCID: PMC6632233] [PubMed: 20220008]

Murphy K, Birn RM, Handwerker DA, Jones TB, Bandettini PA. The impact of global signal regression on resting state correlations: are anti-correlated networks introduced? *Neuroimage* 44: 893–905, 2009a [PMCID: PMC2750906] [PubMed: 18976716]

Murphy M, Riedner BA, Huber R, Massimini M, Ferrarelli F, Tononi G. Source modeling sleep slow waves. *Proc Natl Acad Sci USA* 106: 1608–1613, 2009b [PMCID: PMC2635823] [PubMed: 19164756]

Nelson SM, Dosenbach NU, Cohen AL, Wheeler ME, Schlaggar BL, Petersen SE. Role of the anterior insula in task-level control and focal attention. *Brain Struct Funct* 214: 669–680, 2010 [PMCID: PMC2886908] [PubMed: 20512372]

Nikolic D. Non-parametric detection of temporal order across pairwise measurements of time delays. *J Comput Neurosci* 22: 5–19, 2007 [PubMed: 16998643]

Ogawa S, Lee TM, Kay AR, Tank DW. Brain magnetic resonance imaging with contrast dependent on blood oxygenation. *Proc Natl Acad Sci USA* 87: 9868–9872, 1990 [PMCID: PMC55275] [PubMed: 2124706]

Power JD, Barnes KA, Snyder AZ, Schlaggar BL, Petersen SE. Spurious but systematic correlations in functional connectivity MRI networks arise from subject motion. *Neuroimage* 59: 2142–2154, 2012 [PMCID: PMC3254728] [PubMed: 22019881]

Power JD, Cohen AL, Nelson SM, Wig GS, Barnes KA, Church JA, Vogel AC, Laumann TO, Miezin FM, Schlaggar BL, Petersen SE. Functional network organization of the human brain. *Neuron* 72: 665–678, 2011 [PMCID: PMC3222858] [PubMed: 22099467]

Power JD, Mitra A, Laumann TO, Snyder AZ, Schlaggar BL, Petersen SE. Methods to detect, characterize, and remove motion artifact in resting state fMRI. *Neuroimage* 84: 320–341, 2013 [PMCID: PMC3849338] [PubMed: 23994314]

Purdon PL, Weisskoff RM. Effect of temporal autocorrelation due to physiological noise and stimulus paradigm on voxel-level false-positive rates in fMRI. *Hum Brain Mapp* 6: 239–249, 1998 [PMCID: PMC6873371] [PubMed: 9704263]

Raichle ME. The restless brain. *Brain Connect* 1: 3–12, 2011 [PMCID: PMC3621343] [PubMed: 22432951]

Raichle ME, MacLeod AM, Snyder AZ, Powers WJ, Gusnard DA, Shulman GL. A default mode of brain function. *Proc Natl Acad Sci USA* 98: 676–682, 2001 [PMCID: PMC14647] [PubMed: 11209064]

Raichle ME, Mintun MA. Brain work and brain imaging. *Annu Rev Neurosci* 29: 449–476, 2006 [PubMed: 16776593]

Samann PG, Wehrle R, Hoehn D, Spoormaker VI, Peters H, Tully C, Holsboer F, Czisch M. Development of the brain's default mode network from wakefulness to slow wave sleep. *Cereb Cortex* 21: 2082–2093, 2011 [PubMed: 21330468]

Sato TK, Nauhaus I, Carandini M. Traveling waves in visual cortex. *Neuron* 75: 218–229, 2012 [PubMed: 22841308]

Schacter DL, Buckner RL, Koutstaal W, Dale AM, Rosen BR. Late onset of anterior prefrontal activity during true and false recognition: an event-related fMRI study. *Neuroimage* 6: 259–269, 1997 [PubMed: 9417969]

Schneider G, Havenith MN, Nikolic D. Spatiotemporal structure in large neuronal networks detected from cross-correlation. *Neural Comput* 18: 2387–2413, 2006 [PubMed: 16907631]

Scholvinck ML, Maier A, Ye FQ, Duyn JH, Leopold DA. Neural basis of global resting-state fMRI activity. *Proc Natl Acad Sci USA* 107: 10238–10243, 2010 [PMCID: PMC2890438] [PubMed: 20439733]

Shannon BJ, Dosenbach RA, Su Y, Vlassenko AG, Larson-Prior LJ, Nolan TS, Snyder AZ, Raichle ME. Morning-evening variation in human brain metabolism and memory circuits. *J Neurophysiol* 109: 1444–1456, 2013 [PMCID: PMC3602835] [PubMed: 23197455]

Shulman GL, Pope DL, Astafiev SV, McAvoy MP, Snyder AZ, Corbetta M. Right hemisphere dominance during spatial selective attention and target detection occurs outside the dorsal frontoparietal network. *J Neurosci* 30: 3640–3651, 2010 [PMCID: PMC2872555] [PubMed: 20219998]

Smith SM, Fox PT, Miller KL, Glahn DC, Fox PM, Mackay CE, Filippini N, Watkins KE, Toro R, Laird AR, Beckmann CF. Correspondence of the brain's functional architecture during activation and rest. *Proc Natl Acad Sci USA* 106: 13040–13045, 2009 [PMCID: PMC2722273] [PubMed: 19620724]

Smith SM, Miller KL, Moeller S, Xu J, Auerbach EJ, Woolrich MW, Beckmann CF, Jenkinson M, Andersson J, Glasser MF, Van Essen DC, Feinberg DA, Yacoub ES, Ugurbil K. Temporally-independent functional modes of spontaneous brain activity. *Proc Natl Acad Sci USA* 109: 3131–3136, 2012 [PMCID: PMC3286957] [PubMed: 22323591]

Stokes M, Thompson R, Cusack R, Duncan J. Top-down activation of shape-specific population codes in visual cortex during mental imagery. *J Neurosci* 29: 1565–1572, 2009 [PMCID: PMC6666065] [PubMed: 19193903]

Strick PL, Dum RP, Fiez JA. Cerebellum and nonmotor function. *Annu Rev Neurosci* 32: 413–434, 2009 [PubMed: 19555291]

Sun FT, Miller LM, D'Esposito M. Measuring temporal dynamics of functional networks using phase spectrum of fMRI data. *Neuroimage* 28: 227–237, 2005 [PubMed: 16019230]

Vaishnavi SN, Vlassenko AG, Rundle MM, Snyder AZ, Mintun MA, Raichle ME. Regional aerobic glycolysis in the human brain. *Proc Natl Acad Sci USA* 107: 17757–17762, 2010 [PMCID: PMC2955101] [PubMed: 20837536]

Van Essen DC, Anderson CH, Felleman DJ. Information processing in the primate visual system: an integrated systems perspective. *Science* 255: 419–423, 1992 [PubMed: 1734518]

Vern BA, Leheta BJ, Juel VC, LaGuardia J, Graupe P, Schuette WH. Interhemispheric synchrony of slow oscillations of cortical blood volume and cytochrome aa3 redox state in unanesthetized rabbits. *Brain Res* 775: 233–239, 1997 [PubMed: 9439851]

Vern BA, Leheta BJ, Juel VC, LaGuardia J, Graupe P, Schuette WH. Slow oscillations of cytochrome oxidase redox state and blood volume in unanesthetized cat and rabbit cortex. Interhemispheric synchrony. *Adv Exp Med Biol* 454: 561–570, 1998 [PubMed: 9889936]

Vicente R, Gollo LL, Mirasso CR, Fischer I, Pipa G. Dynamical relaying can yield zero time lag neuronal synchrony despite long conduction delays. *Proc Natl Acad Sci USA* 105: 17157–17162, 2008 [PMCID: PMC2575223] [PubMed: 18957544]

Vincent JL, Patel GH, Fox MD, Snyder AZ, Baker JT, Van Essen DC, Zempel JM, Snyder LH, Corbetta M, Raichle ME. Intrinsic functional architecture in the anaesthetized monkey brain. *Nature* 447: 83–86, 2007 [PubMed: 17476267]

Vyazovskiy VV, Olcese U, Hanlon EC, Nir Y, Cirelli C, Tononi G. Local sleep in awake rats. *Nature* 472: 443–447, 2011 [PMCID: PMC3085007] [PubMed: 21525926]

Yan CG, Cheung B, Kelly C, Colcombe S, Craddock RC, Di Martino A, Li Q, Zuo XN, Castellanos FX, Milham MP. A comprehensive assessment of regional variation in the impact of head micromovements on functional connectomics. *Neuroimage* 76: 183–201, 2013 [PMCID: PMC3896129] [PubMed: 23499792]

Yeo BT, Krienen FM, Sepulcre J, Sabuncu MR, Lashkari D, Hollinshead M, Roffman JL, Smoller JW, Zollei L, Polimeni JR, Fischl B, Liu H, Buckner RL. The organization of the human cerebral cortex estimated by intrinsic functional connectivity. *J Neurophysiol* 106: 1125–1165, 2011 [PMCID: PMC3174820] [PubMed: 21653723]

Yuste R. Introduction: spontaneous activity in the developing central nervous system. *Semin Cell Dev Biol* 8: 1–4, 1997 [PubMed: 15001098]

Zhang D, Raichle ME. Disease and the brain's dark energy. *Nat Rev Neurol* 6: 15–28, 2010 [PubMed: 20057496]

Figures and Tables

Fig. 1.
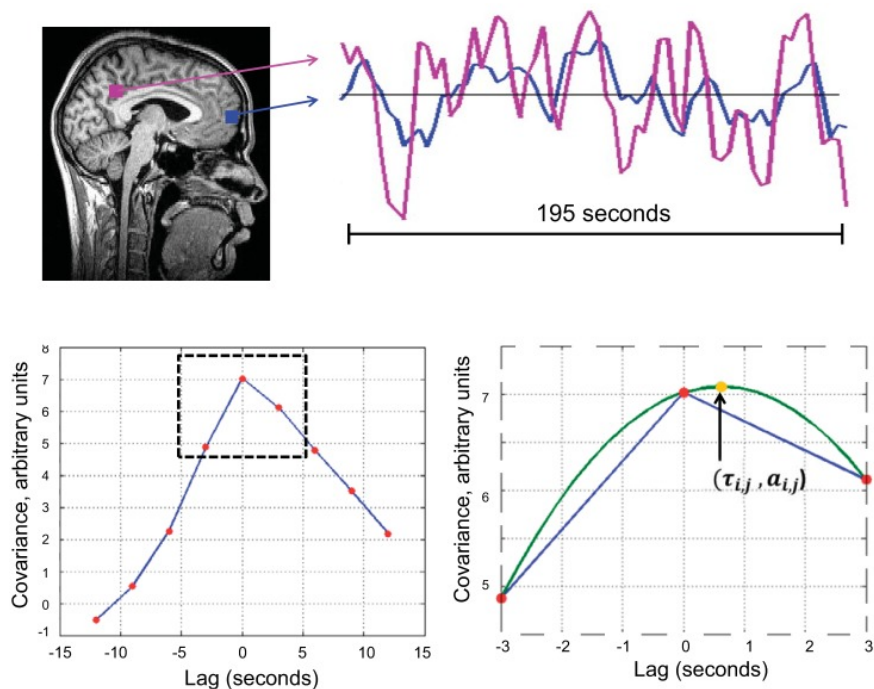
Calculation of pairwise time series lag using cross-covariance and parabolic interpolation. *Top*: 195 s of 2 sampled time series extracted from 2 loci in the brain. *Bottom left*: the corresponding lagged cross-covariance function, computed over a full run (~300 s) (*Eq. 2*). The lagged cross-covariance is defined over the range ±L, where L is the run duration. The range of the plotted values is restricted to ±12 s, which is equivalent to ±4 frames (red markers) when the repetition time is 3 s. The lag between the time series is the value at which the [absolute value of the] cross-covariance function is maximal. This extremum can be determined at a resolution finer than the temporal sampling density (1 frame every 3 s) by performing parabolic interpolation (green line, *bottom right*) through the computed values (red markers). This extremum (arrow, yellow marker) defines both the lag between time series i and j ($\tau_{i,j}$; *Eq. 4*) and the corresponding amplitude ($a_{i,j}$; *Eq. 5*).

Table 1.

Characteristics of analyzed data sets

	Data Set			
	1	*2*	*3*	*4*
No. of subjects	692 (305 M + 387 F)	10 (4 M + 6 F)	17 (8 M + 9 F)	24 (15 M + 9 F)
Age, yr	21.4 ± 2.4 (SD)	23.3 ± 3 (SD)	23.1 ± 2.4 (SD)	25.9 ± 2.3 (SD)
Scanner	Siemens Tim Trio	Siemens Allegra	Siemens Allegra	Siemens Tim Trio
Acquisition voxel size	$(3 \text{ mm})^3$	$(4 \text{ mm})^3$	$(4 \text{ mm})^3$	$(4 \text{ mm})^3$
Flip angle, °	85	90	90	90
Repetition time, s	3.00	3.03	2.16	2.08
No. of frames	124 × 2 runs	110 × 6 runs	194 × 2 runs	194 × 2 runs
Citation	Yeo et al. (2011)	Fox et al. (2005b)	Fox et al. (2007)	Shannon et al. (2012)
Experimental question	Replicability	Eyes open vs. eyes closed	Before vs. after motor task	Morning vs. evening

Fig. 2.
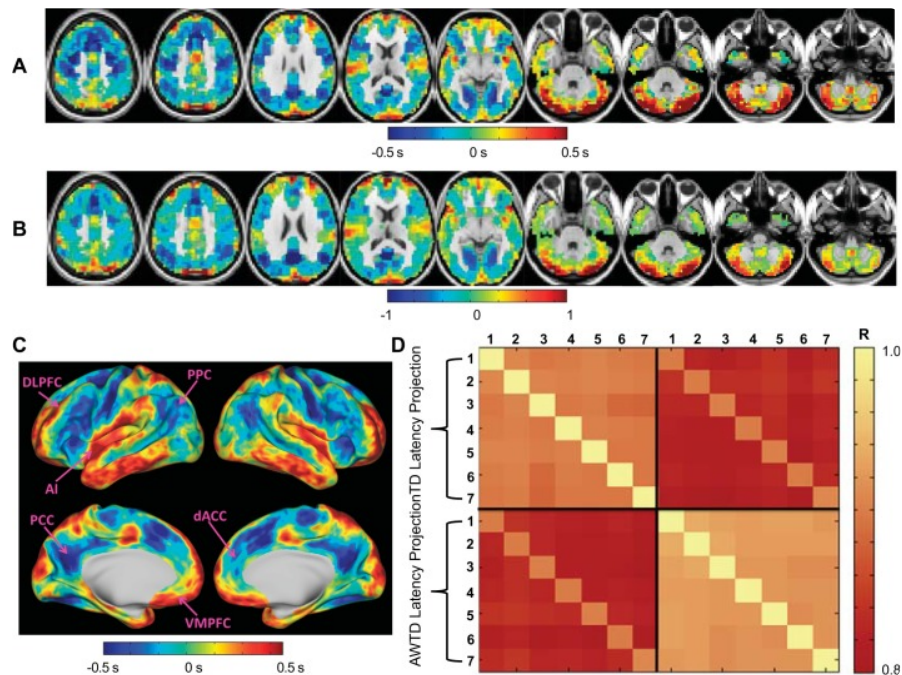
Results obtained in *data set 1*. The 692 subjects were randomly divided into 7 equally sized subgroups of ~99 subjects each. *A*: latency projection of the time-delay (TD) result obtained in the first subgroup illustrated in voxel-space. Lag is measured in seconds. *B*: latency projection of the amplitude-weighted time-delay (AWTD) result corresponding to the TD result shown in *A*. Because the blood oxygen level-dependent (BOLD) signal magnitude depends on multiple fMRI sequence parameters, the unit of amplitude-weighted lag is arbitrary. *C*: surface representation of the volumetric result shown in *A*. Arrows point to specific regions mentioned in DISCUSSION: posterior precuneus cortex (PCC), ventromedial prefrontal cortex (VMPFC), dorsal anterior cingulate cortex (dACC), anterior insula (AI), posterior parietal cortex (PPC), and dorsolateral prefrontal cortex (DLPFC). *D*: spatial correlation between all TD (first 7 rows/columns) and AWTD (last 7 rows/columns) latency projections calculated in the 7 subgroups.

Fig. 3.
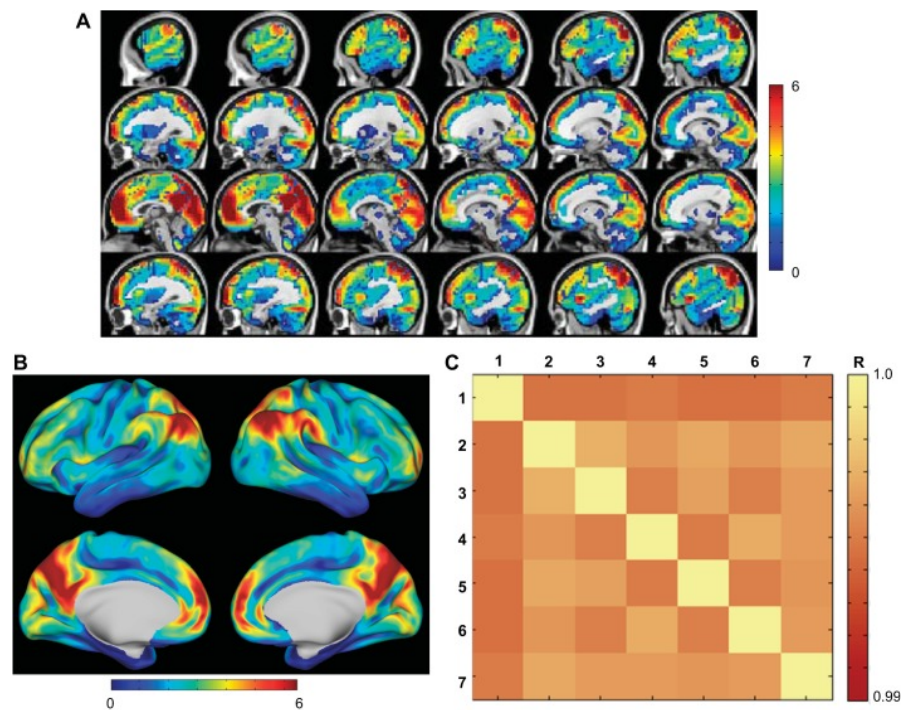
A: latency process amplitude (LPA) map illustrated in voxel-space obtained in the first subgroup of *data set 1* (same data as in Fig. 2, *A–C*). The scale is in units of BOLD amplitude. See *Eq. 8* for derivation. *B*: surface representation of the volumetric result shown in *A*. *C*: spatial correlation between all amplitude maps calculated in the 7 subgroups of *data set 1*.

Fig. 4.
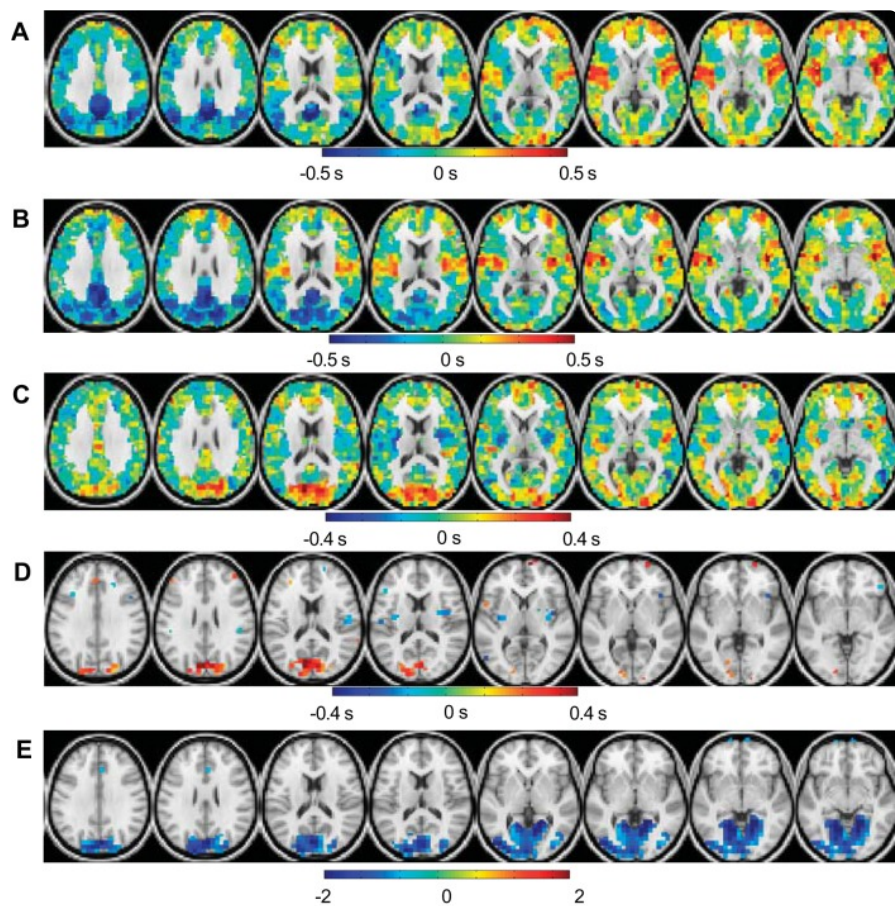
Latency results obtained in *data set 2*. *A*: eyes open (EO). *B*: eyes closed (EC). *C*: EO minus EC. *D*: voxels with a statistically significant EO vs. EC latency effect. *E*: EO minus EC LPA difference image. Color indicates statistically significant voxels.

Fig. 5.
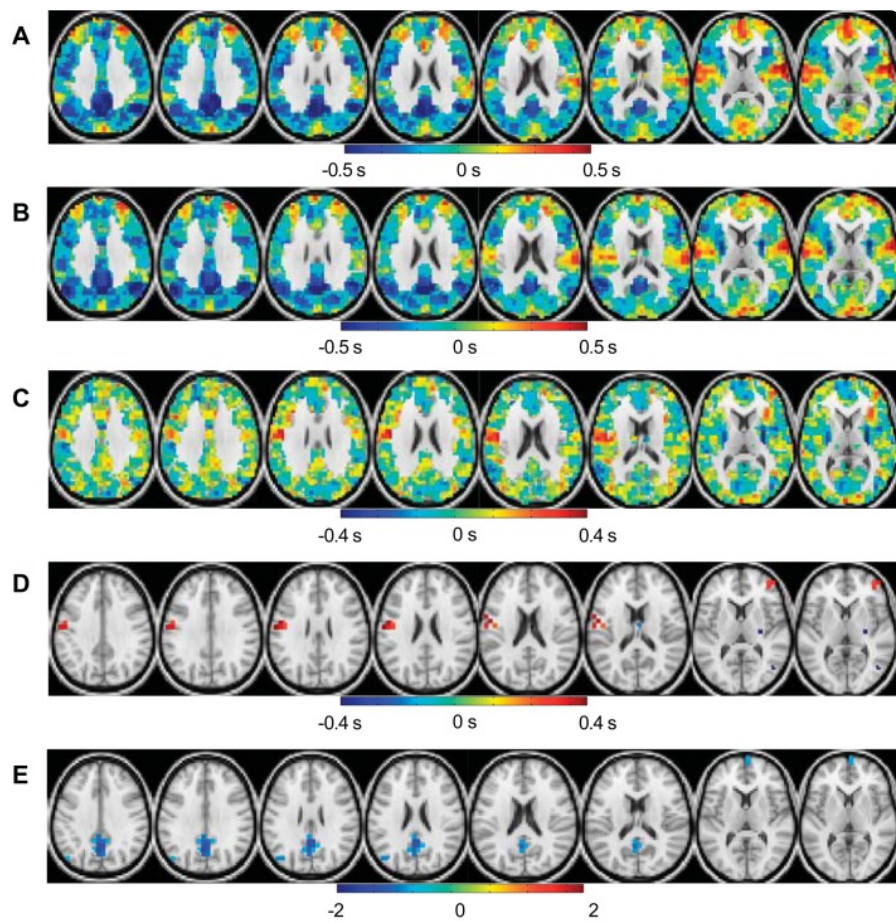
Latency results obtained in *data set 3*. *A*: before button-press task. *B*: after button-press task. *C*: after minus before. *D*: voxels with a statistically significant recent task performance latency effect. *E*: after minus before LPA difference image. Color indicates statistically significant voxels.

Fig. 6.
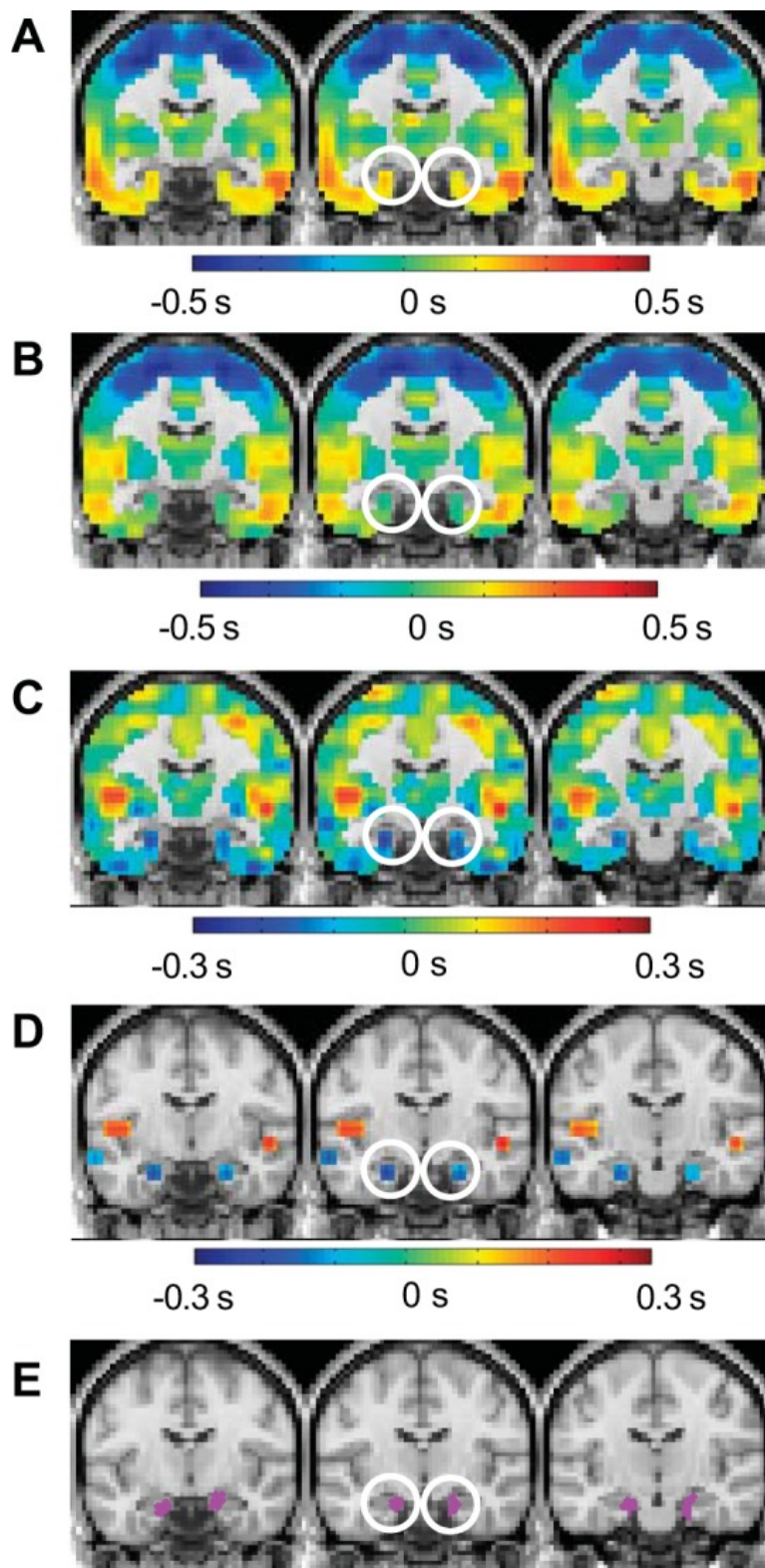
Latency results obtained in *data set 4*. *A*: morning latency map. *B*: evening latency map. *C*: evening minus morning change in latency. Warm hues indicate increased lateness in the evening. Cool hues indicate increased earliness in the evening. *D*: statistically significant latency differences are seen in entorhinal and insular cortex. *E*: previously reported (Shannon et al. 2013) diurnal change in functional connectivity. Magenta indicates the 2 regions of interest, right and left entorhinal cortex,

exhibiting the greatest diurnal change in functional connectivity with the rest of the brain (circled in central slices in *A–E*). Presently reported diurnal changes in latency (*A–D*) correspond to previously published functional connectivity changes in entorhinal cortex (*E*).
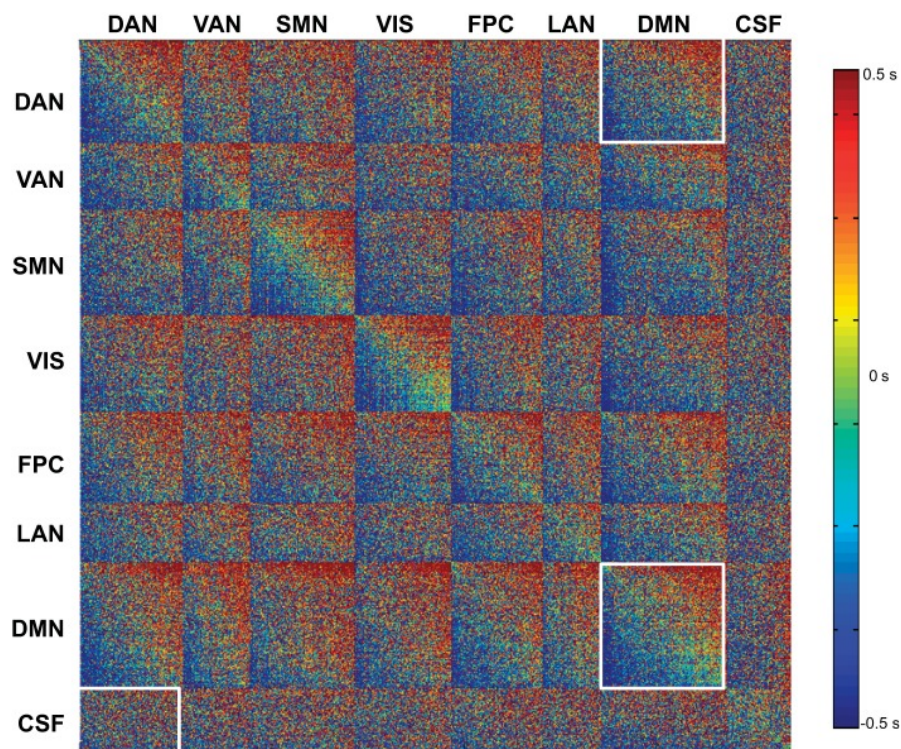
Fig. 7.
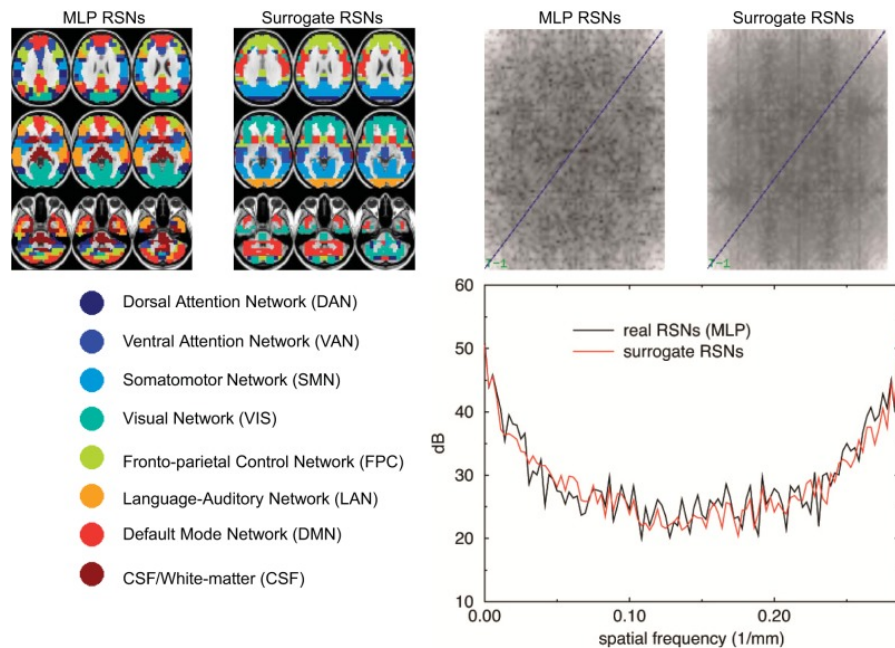
Real and surrogate resting-state networks (RSNs). RSN labels and color codes are presented at *bottom left*. To test the statistical significance of the latency-RSN relationship, we created surrogate RSNs matched in spatial frequency to real RSNs. The real RSNs were defined as the group-level winner-take-all result in Hacker et al. (2013) (referred to here as "MLP RSNs"). Surrogate RSNs (*n* = 1,000) were generated by applying symmetric group operations to the real RSNs (see APPENDIX). One typical example of surrogate RSNs is illustrated adjacent to the real RSNs. Spatial frequency domain representations (3D Fourier transforms of RSNs and surrogate RSNs) are at *top right*. The spatial frequency domain results are averaged over all real RSNs and over all surrogate RSNs, respectively, omitting the cerebrospinal fluid (CSF) component. Only the $f_z = 0$ planes of the 3D spatial frequency domain representations are shown. The graph (*bottom right*) shows relative spectral power (in dB) read out along the diagonal blue traces in the frequency domain representations. The plots are symmetric about the Nyquist folding frequency = 0.53 mm, which reflects the spatial sampling density (3-mm cubic voxels). Critically, the spatial frequency content of the surrogate RSNs is well matched to the real RSNs.

Fig. 8.
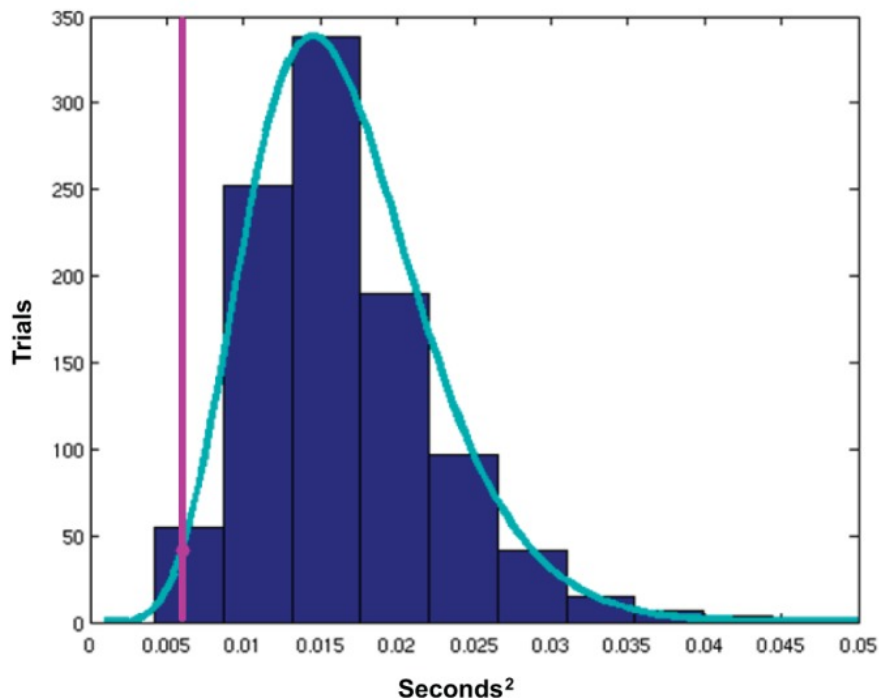
Histogram of summed squared mean latency values in surrogate RSNs. One thousand surrogate RSN partitions (e.g., Fig. 7) were generated. The latency mean was evaluated for each surrogate RSN. On the assumption that mean RSN latencies are normally distributed about zero, the sum of squares of these values theoretically is distributed as $\chi^2(7)$. The light blue trace represents the theoretical gamma probability density function fit to the simulations (blue histogram). The vertical pink line represents the summed squared latency values in the real RSNs (0.006 s^2). A squared sum value of 0.006 s^2 corresponds to a root mean square value of 0.03 s, as reported in the text. The surrogate data indicate that the probability of this outcome occurring by chance is $P < 0.0096$.

Fig. 9.

Relationship of latency to RSNs. Figure shows a TD matrix with regions of interest (ROIs) ordered by RSN membership (see Fig. 7 for abbreviations). Within each RSN, the ROIs are further ordered by latency. Note wide range of latencies within RSNs (diagonal blocks, each necessarily anti-symmetric) and anti-symmetric features across RSNs (off-diagonal blocks). Note also absence of organization in CSF blocks. Blocks referred to in the main text are outlined in white. The diagonal blocks in the TD matrix illustrate that each network has early, middle, and late components. Moreover, the off-diagonal blocks have early, middle, and late components. Therefore, no network leads or follows any other network. Rather, lags are equivalently distributed within and across RSNs.

Fig. 10.
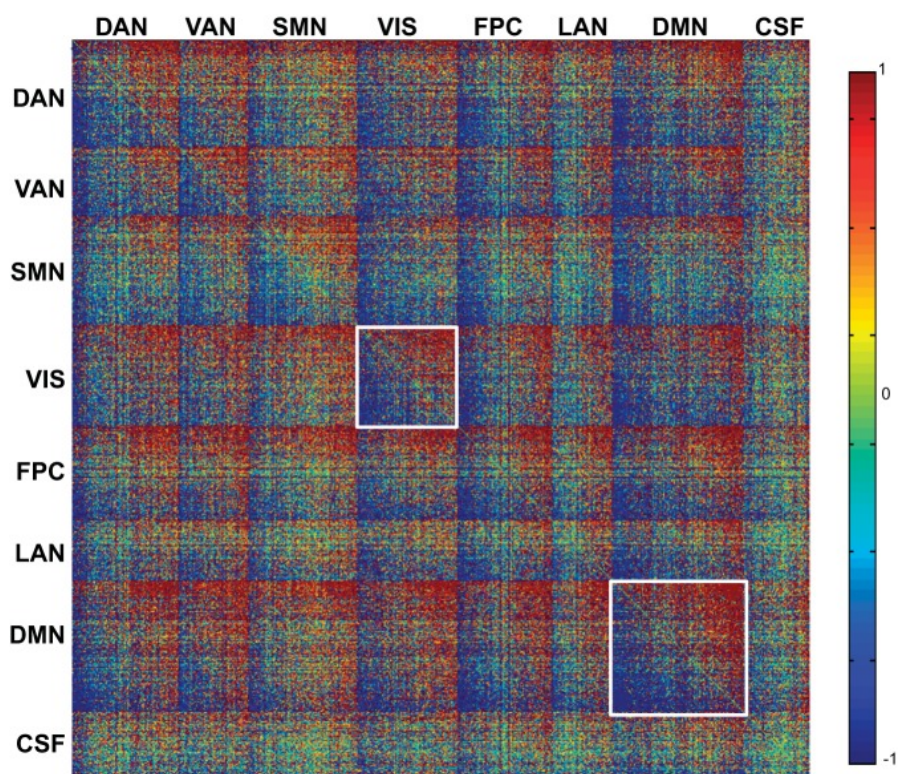
AWTD matrix corresponding to Fig. 9. Blocks referred to in the main text are outlined in white.

Fig. 11.
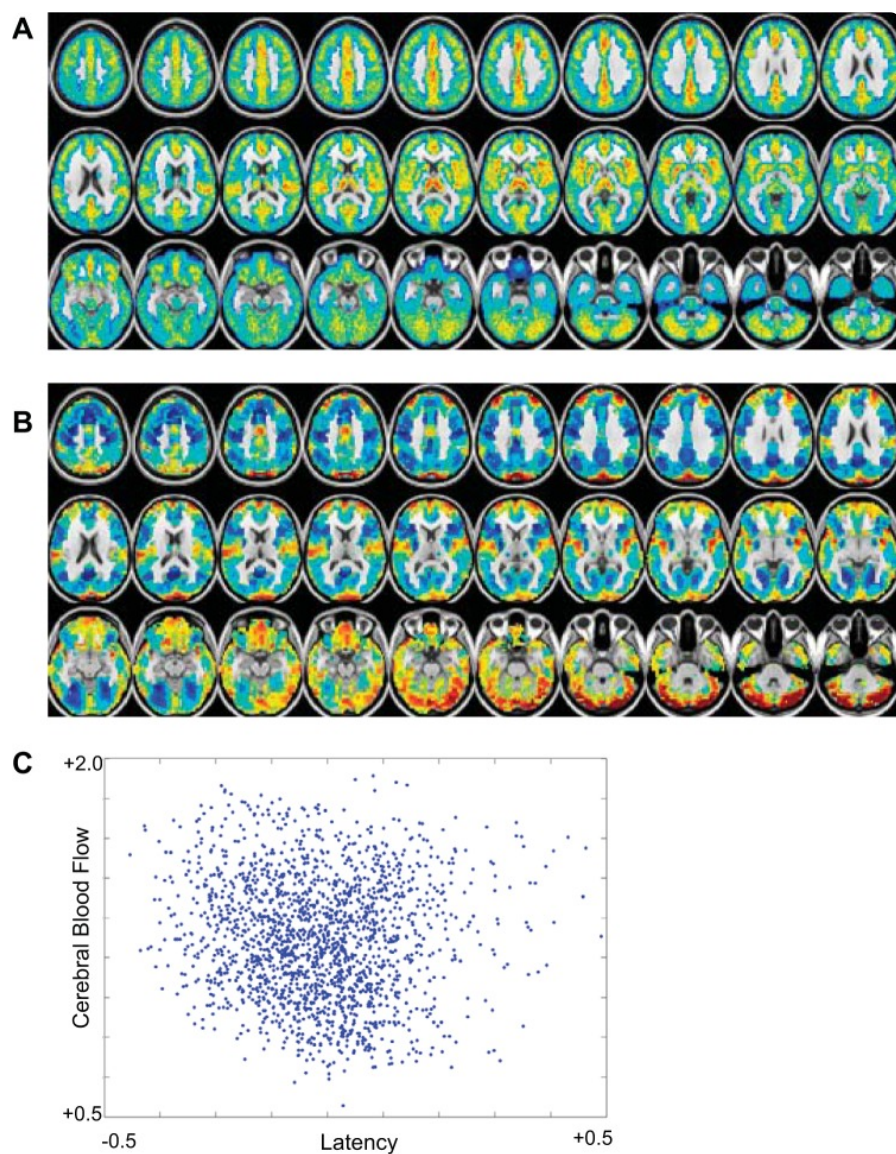
Comparison of cerebral blood flow (CBF) vs. TD latency projection. *A*: CBF map obtained in a group of 33 normal young adults. *B*: TD latency projection; same data as Fig. 2, *A–C*. *C*: scatterplot showing the relationship between CBF and the latency projection. Each dot represents 1 ROI. To test whether the reproducibility of latency structure (Fig. 2D) is attributable to CBF, we computed the mean cross-group correlation for the 7 cohorts in *data set 1*, before and after regressing out the effects of CBF. The mean cross-group correlation was $r = 0.898$ in both cases. This result demonstrates that the effect of CBF on measured latency, if present, is negligible.

Fig. 12.
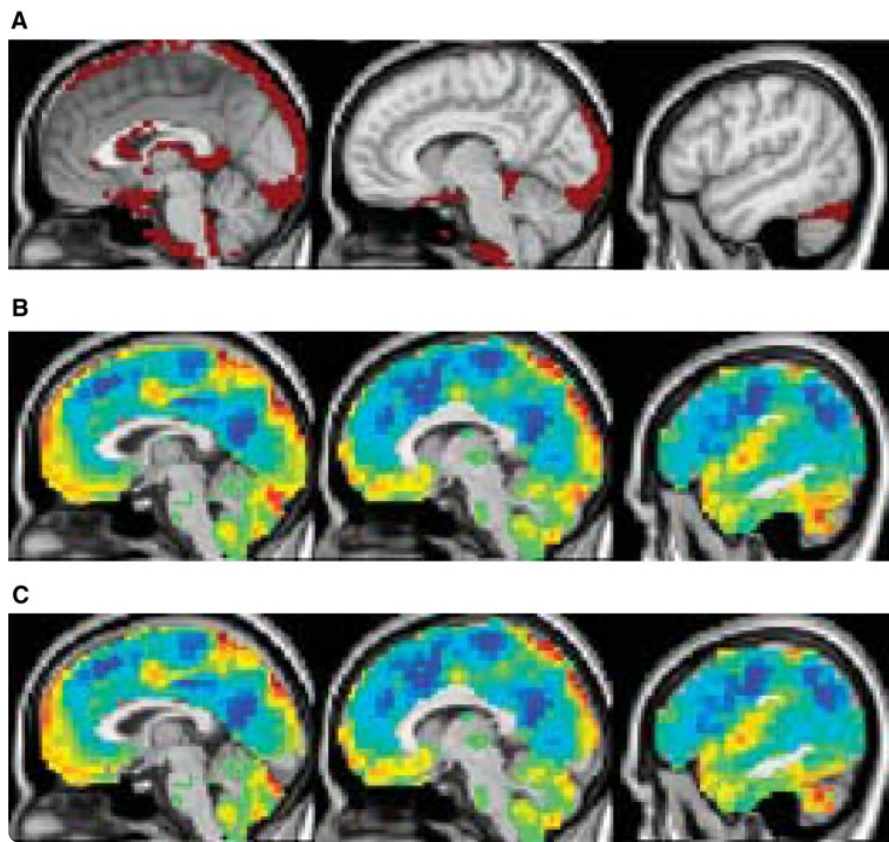
Venous contribution to latency structure. *A*: venogram. *B*: TD latency projection for comparison. Our gray matter masking procedure (see IMAGING METHODS) excludes many of the voxels that correspond to venous structures, but some overlap is apparent. *C*: TD latency projection with venous structures masked out.

Fig. 13.
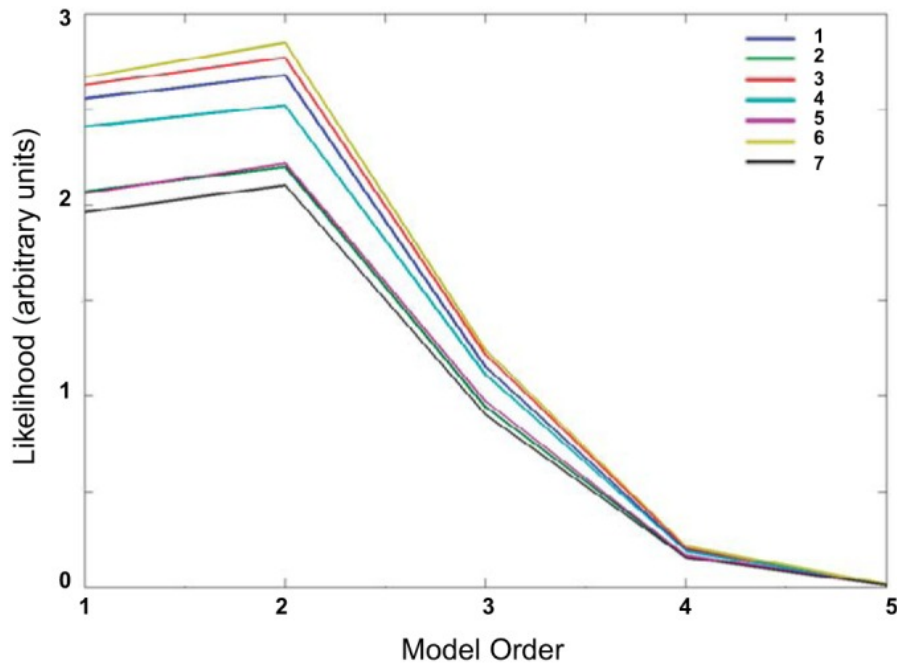
Estimation of TD matrix model order. The TD matrix intrinsic dimensionality likelihood was calculated (Minka 2001) with the Bayesian information criterion (BIC) in the 7 groups corresponding to Fig. 2. In each group, the dimensionality of highest likelihood is 2. This result implies the existence of 2 transitive systems of lags within the TD matrix. Regionally dependent neurovascular coupling can explain only 1 of these transitive systems of lags. Therefore, hemodynamic delays, even if they are substantial, cannot account for the entirety of latency structure.